

RGBlimp-Q: Robotic Gliding Blimp With Moving Mass Control Based on a Bird-Inspired Continuum Arm

Hao Cheng and Feitian Zhang

Abstract—Robotic blimps, as lighter-than-air aerial platforms, offer extended operational duration and enhanced safety in human-robot interactions due to their buoyant lift. However, achieving robust flight performance under environmental airflow disturbances remains a critical challenge, thereby limiting their broader deployment. Inspired by avian flight mechanics, particularly the ability of birds to perch and stabilize in turbulent wind conditions, this article introduces RGBlimp-Q—a robotic gliding blimp equipped with a bird-inspired continuum arm featuring a novel moving mass actuation mechanism. This continuum arm enables flexible attitude regulation through internal mass redistribution, significantly enhancing the system’s resilience to external disturbances. Additionally, it facilitates aerial manipulation by employing end-effector claws that interact with the environment in a manner analogous to avian perching behavior. This article presents the design, modeling, and prototyping of RGBlimp-Q, supported by comprehensive experimental evaluation and comparative analysis. To the best of the authors’ knowledge, this represents the first interdisciplinary integration of continuum mechanisms into a lighter-than-air robotic platform, where the continuum arm simultaneously functions as both an actuation and manipulation module. This design establishes a novel paradigm for robotic blimps, expanding their applicability to complex and dynamic environments.

Index Terms—Aerial Systems: Mechanics and Control, Flying Robots, Mechanism Design.

I. INTRODUCTION

WITH the growing demand for aerial vehicle applications, there is an increasing need for portable miniature aerial robots capable of low-speed, safe, and long-endurance flight [1]–[3]. In recent years, significant attention has been directed towards the development of robotic blimps, owing to their extended flight endurance and enhanced safety during human-robot interactions [4]–[11]. As a type of lighter-than-air (LTA) aerial vehicle, robotic blimps offer substantial potential for applications that require prolonged airborne operation at low speeds. Examples include search and rescue missions [6], [12], environmental monitoring [13], [14], human-robot interaction [15]–[17], and entertainment [18], [19]. Unlike heavier-than-air (HTA) aircraft, robotic blimps leverage buoyancy

This research was in part supported by the National Natural Science Foundation of China under Grant 62473006. (Corresponding author: Feitian Zhang.)

The authors are with the Robotics and Control Laboratory, School of Advanced Manufacturing and Robotics, and the State Key Laboratory of Turbulence and Complex Systems, Peking University, Beijing, 100871, China (e-mail: h-cheng@stu.pku.edu.cn; feitian@pku.edu.cn).

The videos, open-sourced hardware, and source code of this work are available at <https://RGBlimp.github.io>.



Fig. 1. A snapshot of the RGBlimp-Q perching on a branch through the use of the novel continuum arm design (the upper figure), emulating the behavior of a bird, as shown in the lower figure [20].

to counteract gravity, resulting in reduced energy consumption. However, their buoyant nature makes them particularly sensitive to airflow disturbances, which poses a significant challenge to achieving robust flight, especially in complex outdoor environments. Therefore, enhancing the flight stability and robustness of robotic blimps is crucial to fully realizing their potential for long endurance and safe operation.

Numerous efforts in the literature have focused on achieving robust flight for robotic blimps by employing disturbance compensation controllers while maintaining the conventional omnidirectional thrust actuation mechanism [21]–[24], a method commonly used in rotary-wing aerial robots [25]–[28]. With the advancement of rotary-wing aerial robots, significant progress has been made in the robust flight control of small-sized aerial vehicles. Notable examples include neural network-based disturbance estimators for robust flight control of quadrotors [25], uncertainty-aware model predictive controllers for mitigating wind and payload disturbances in multi-rotor systems [26], [27], and controllers compensating for aerodynamic disturbances caused by ground effects [28]. Building on methodologies from rotary-wing systems, disturbance compensation strategies for indoor robotic blimps have been demonstrated. These include Luenberger observer design for disturbance estimation [21], wind effect mitigation via reinforcement learning [23], wind-aware motion planning

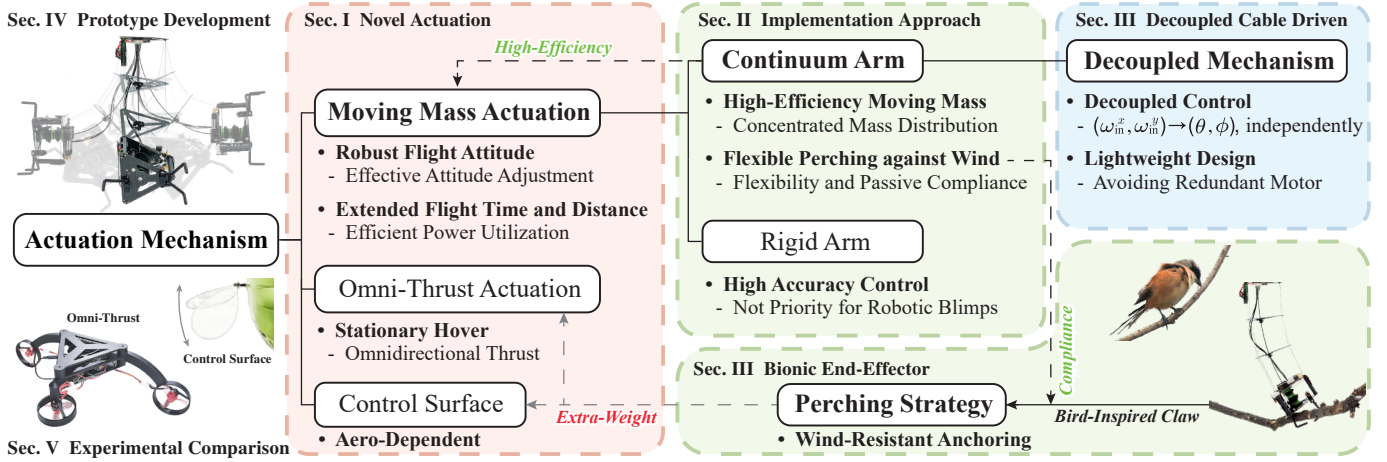


Fig. 2. The hierarchical block diagram illustrating the structure of this article and the contributions of the proposed RGBlimp-Q design. Section I introduces the moving mass actuation mechanism for RGBlimp-Q, which enables both effective attitude adjustment and efficient energy utilization. This mechanism distinguishes RGBlimp-Q from conventional blimps, supporting sustained flight over extended time and distance for tasks such as indoor inspection and outdoor monitoring. Section II proposes the continuum mechanism as an efficient implementation of moving mass actuation. This mechanism is seamlessly integrated into the LTA aerial system to enhance moving mass actuation and enable perching capability through the end-effect claw. Section III presents a lightweight, decoupled cable-driven mechanism designed to accommodate the limited payload capacity of robotic blimps. Section IV showcases the developed RGBlimp-Q prototype, equipped with the continuum arm. Section V outlines indoor and outdoor flight experiments that validate the proposed design’s effectiveness in attitude adjustment and energy utilization, demonstrating superior performance compared to conventional omnidirectional thrust mechanisms. Furthermore, the reliability and repeatability of the continuum arm were confirmed through an 18-hour endurance test involving 3,000 repeated flight cycles.

using dynamic programming [24], and attitude stabilization with dual-loop control [29]. However, significant performance distinctions between robotic blimps and rotary-wing aerial robots, such as differences in aerodynamics and actuation mechanisms, have been underexplored. Consequently, (almost) all robust controllers based on the existing mechanism design of robotic blimps face challenges in achieving the robust outdoor flight performance seen in rotary-wing aerial robots. The mechanism design, particularly the actuation mechanism, specifically tailored for robotic blimps to enable robust flight has long been neglected. This oversight has hindered the successful application of robust flight control techniques to robotic blimps, preventing them from achieving the outdoor flight capabilities that rotary-wing aerial robots have demonstrated in windy environments. To address this challenge, it is essential to design a novel actuation mechanism for robotic blimps that enables robust flight performance.

In the natural world, flying lizards and flying squirrels utilize the inertia of their tails to control their gliding attitude, particularly during low-speed flight [30], [31]. Similarly, birds exhibit robust flight by dynamically adjusting their wing movements to alter their attitude in response to wind disturbances [32], [33] and by using their claws to perch on branches, effectively resisting excessive wind [34], [35]. In contrast, current robotic blimps lack an adaptive mechanism analogous to these natural strategies, limiting their ability to withstand wind disturbances.

With the rise of bio-inspired robotics [36] and aerial robotic manipulation [1], [2], significant progress has been made in the perching capabilities of rotary-wing aircraft. This progress focuses on enabling perching on support structures using manipulators, including bio-inspired passive mechanisms and actively controlled grippers [34], [37]–[39]. Examples include modular quadrotor landing gear [37], bio-inspired robotic legs with grippers for rotary-wing drone perching [34], and eagle-

like claws for object capture in fixed-wing robots [40].

While rigid-arm-based aerial robotic manipulations remain dominant in the literature, continuum arms present a promising alternative due to their compact structure, lightweight design, and agile motion capabilities. This innovative concept incorporates flexible backbone structures with theoretically infinite degrees of freedom [41]–[43], utilizing various backbone materials such as elastic materials [44]–[48], and actuated by pneumatic or cable-driven mechanisms [45]–[48]. To manage the inherent complexity of continuum arms, the piecewise constant curvature (PCC) kinematics is commonly employed [48]–[51]. Recent advancements have further integrated aerial continuum manipulators onto quadrotors to facilitate grasping operations [52], [53].

However, the integration of such mechanisms onto robotic blimps remains largely unexplored. Given the inherent advantages of long endurance and low-speed flight, as well as the challenges posed by vulnerability to disturbances, the introduction of such mechanisms for aerial manipulation or perching in wind is both appropriate and essential for enhancing the functionality of LTA aerial systems. A significant challenge therein lies in the mismatch between the weight of existing manipulators and the limited payload capacity of robotic blimps.

This article introduces RGBlimp-Q, **the first** robotic gliding blimp equipped with a bionic, lightweight continuum arm designed for both moving mass control and object capture. Building upon our previous work on RGBlimp [7], which utilized hybrid aerodynamic-buoyant lift, RGBlimp-Q integrates a lightweight continuum arm with a bird-like claw. This bird-inspired continuum arm not only enables flexible spatial moving mass control, thereby enhancing effective attitude adjustment in the air, but also facilitates object grasping, mimicking the behavior of birds. This design addresses a

critical yet often overlooked requirement for station-keeping operations and wind-resistant anchoring in robotic blimps. A prototype of RGBlimp-Q is developed, weighing approximately 7g, accounting for net buoyancy. Extensive flight experiments, conducted both indoors and outdoors using a classical feedback controller, validate the effectiveness of the proposed design in improving flight maneuverability and robustness. As illustrated in Fig. 2, the contributions of this article are twofold:

1) *Novel actuation mechanism*: This article introduces the RGBlimp-Q design, a novel robotic blimp featuring a unique moving mass actuation mechanism for attitude adjustment. The proposed design aims to extend the advantages of robotic blimps to complex, disturbed environments. It enables both effective attitude control and efficient energy utilization, facilitating robust and durable flight over time and distance.

2) *Bird-inspired continuum arm*: The proposed bird-inspired continuum arm enhances moving mass actuation through concentrated mass distribution and enables object capture via the end-effector claw. This allows the robot to maintain stable flight or perch against disturbances, mimicking bird behavior. Additionally, a decoupled cable-driven mechanism is introduced to achieve a lightweight design and decoupled control in robotic blimps. This integration marks the first organic combination of a continuum mechanism and a cable-driven system in robotic blimp platforms.

The aforementioned contributions are validated through systematic indoor and outdoor physical flight experiments, which demonstrate enhanced robustness in flight attitude, extended flight time and distance, and improved adaptability to complex environments with disturbances.

The rest of this article is organized as follows. Section II presents the RGBlimp-Q design with improved flight attitude adjustment capability through moving mass actuation. Such novel actuation, implemented via a continuum arm, marks the first integration into an LTA system. Section III proposes the lightweight-oriented decoupled cable-driven continuum arm with an end-effect claw for both effective attitude control and resisting wind disturbances. Section IV presents the developed RGBlimp-Q prototype and provides system identification results. Section V describes indoor and outdoor flight experiments that validate the effectiveness of the proposed design in both attitude adjustment and energy utilization, outperforming conventional omnidirectional thrust mechanisms. Moreover, the reliability and repeatability of the proposed continuum arm are validated through a repeated motion test exceeding 3000 cycles and 18 hours. Finally, Section VI concludes this article and discusses potential improvements.

II. RGBLIMP-Q WITH MOVING MASS ACTUATION

To enable low-speed, long-duration flight in both indoor and outdoor environments while improving robustness against wind disturbances, we propose RGBlimp-Q, a robotic gliding blimp actuated via moving mass control. Our prior work on RGBlimp [7] demonstrated the critical role of aerodynamic optimization, such as the integration of wings and tail-planes, in enhancing the performance of robotic blimps. These enhancements were validated through aerodynamic analysis and

empirical evaluation. Building upon these findings, achieving further aerodynamic robustness necessitates enhanced attitude adjustment capabilities. This is due to the sensitivity of flight dynamics to aerodynamic angles, specifically the angle of attack (α) and sideslip angle (β), both of which are affected by the vehicle's attitude and environmental wind conditions (wind direction and strength). This section investigates the advantages of the moving mass control approach, focusing on its impact on flight maneuverability and robustness. It begins with an introduction to the moving mass actuation mechanism, highlighting the benefits of using the continuum mechanism for moving mass implementation. The section then presents the first-principle dynamic model of the RGBlimp-Q, which incorporates continuum-based moving mass actuation. To ensure generalization, the dynamics modeling is structured hierarchically, progressing from the general motion dynamics that account for moving mass actuation (Section II-B) to continuum-specific mechanics (Section II-C and Section II-D), and concluding with the decoupled cable-driven control (Section III-A and Section III-B).

A. Moving Mass Actuation for Flight Attitude Adjustment

The moving mass actuation mechanism has historically been overlooked in the design of robotic blimps. Previous design of robotic blimps in the literature often treated the non-negligible distance between the center of gravity (CG) and the center of buoyancy (CB) as a drawback and sought to mitigate its effects, such as swing-reducing control [29]. Emerging research has shown the advantages of this inherent property. For example, Xu *et al.* systematically utilize the inherent CG-CB distance to generate stabilizing swing moments for translational control [11]. In contrast, we hypothesize that transforming this fixed distance into a variable facilitates attitude adjustment and is achievable through moving mass control.

This article proposes a unique robotic blimp design based on the moving mass actuation mechanism for improved attitude adjustment capability, distinguishing it from existing robotic blimps utilizing omnidirectional thrusters. This design leverages the gravitational moment associated with the variable spatial distance between CG and CB to effectively control the attitude of a robotic blimp, especially during low-speed flight. Conventional control surfaces, such as the rudder, elevator, and aileron, commonly used in high-speed aerial vehicles such as fixed-wing aircraft, exhibit significantly reduced effectiveness in controlling low-speed robotic blimps. This limitation comes from the dependence of aerodynamic effects on dynamic pressure, e.g., $\|M\| \propto \rho V^2$, where M represents the aerodynamic moment, ρ represents air density, and V stands for the relative airspeed, equivalent to the cruising speed in calm environmental conditions.

To achieve moving mass control, we employ a fixed-length continuum arm with two degrees of freedom (DoF), operating under the constant curvature (CC) assumption. This continuum mechanism, characterized by a compact mass distribution, enhances the attitude adjustment capabilities within the context of moving mass actuation for robotic blimps. It is identified

as a crucial design choice for the RGBlimp-Q, and detailed in Section II-C. To illustrate, we examine roll angle $\phi \in (-90^\circ, 90^\circ)$ adjustment, which is applicable to pitch as well, through a comparative study of moving mass actuation using continuum versus rigid mechanisms, as shown in Fig. 3.

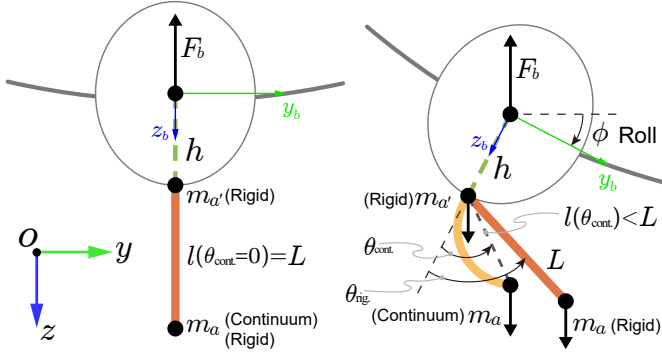


Fig. 3. Illustration of reference frames, forces, and key variables for theoretical comparison of roll adjustment via moving mass actuation: continuum arm (compact with concentrated mass m_a) versus rigid arm (with m_a and joint actuator mass $m_{a'}$). Initially, both arms have zero rotation angle, i.e., $\theta_{\text{cont}} = \theta_{\text{rig}} = 0$, resulting in a roll angle $\phi = 0$ (left). Gravity balance is achieved by moment equilibrium, i.e., $\tau_{m_{a'}} + \tau_{m_a} = 0$ for the rigid arm, while $\tau_{m_a} = 0$ for the continuum arm (right).

The comparative analysis is based on an idealized model wherein the blimp's center of gravity (CG) coincides with its center of buoyancy (CB), thereby isolating the manipulator's influence on moment generation. Under this assumption, we compare actuation efficiency between a continuum arm modeled as a single moving mass m_a at its end and a rigid arm comprising the same m_a plus an additional joint actuator mass $m_{a'}$. Both arms are mounted at a distance h below CG (CB) and have the same constant length L . To ensure physically meaningful comparisons, the rotational angles θ_{cont} and θ_{rig} , as actuation inputs, are constrained within the operational range of $[-60^\circ, 60^\circ]$.

The constraint equation for the rigid arm, considering the equilibrium of gravitational moments, is derived as follows

$$\cot \phi_{\text{rig}} = -\cot \theta_{\text{rig}} - (1 + k_m^{\text{rig}}) k_l^{\text{rig}} \csc \theta_{\text{rig}}, \quad (1)$$

where the coefficient $k_m^{\text{rig}} = m_{a'}/m_a \geq 0$ and $k_l^{\text{rig}} = h/L > 0$.

In contrast, the CC assumption and the concentrated mass distribution of the continuum arm imply that its equilibrium is governed by geometric relations. Consequently, the constraint equation for the continuum arm related to the arc chord length $l(\theta_{\text{cont}})$ is given by

$$\cot \phi_{\text{cont}} = -\cot \theta_{\text{cont}} - k_l^{\text{cont}} \theta_{\text{cont}} \csc^2 \theta_{\text{cont}}, \quad (2)$$

where the coefficient $k_l^{\text{cont}} = h/l(\theta_{\text{cont}}) > 0$.

Expanding Eqs.(1) and (2), the first-order approximation of these constraint equations show a negligible error of approximately $\pm 3^\circ$, computed as

$$\phi_{\text{cont}} = -K_{\text{cont}} \theta_{\text{cont}}, \quad \phi_{\text{rig}} = -K_{\text{rig}} \theta_{\text{rig}}, \quad (3)$$

Here, the coefficients K_{cont} and K_{rig} represent the scaling factors for the continuum and rigid arms, respectively. These

factors quantify the extent to which the rotational angles of the arms influence the roll angle, calculated as

$$K_{\text{cont}} = \frac{1}{(1 + k_m^{\text{cont}})}, \quad K_{\text{rig}} = \frac{1}{1 + (1 + k_m^{\text{rig}}) k_l^{\text{rig}}}.$$

We compare the attitude adjustment capabilities by analyzing K_{cont} and K_{rig} under the condition that $\theta_{\text{cont}} = \theta_{\text{rig}}$. Given the same arm length L and displacement h in Eq. (3), the continuum arm exhibits a higher gain due to its concentrated mass distribution. Specifically, K_{cont} is independent of k_m , leading to a greater gain K_{cont} compared to K_{rig} , as $k_m^{\text{rig}} = m_{a'}/m_a > 0$ for rigid arms. For example, with parameters $L = 0.40$ m, $h = 0.30$ m, $m_a = 30$ g, and $m_{a'} = 15$ g, $K_{\text{cont}} \approx 0.57$, $K_{\text{rig}} \approx 0.47$, indicating an approximately 21.3% improvement in attitude adjustment achieved by the continuum actuation mechanism. For maximum input rotation angles $\theta_{\text{cont}} = \theta_{\text{rig}} = \pm 60^\circ$, the resulting roll angles are $|\phi_{\text{cont}}| = 34.2^\circ$ and $|\phi_{\text{rig}}| = 28.2^\circ$, respectively. Furthermore, for the same attitude angle $\phi_{\text{cont}} = \phi_{\text{rig}}$ (as Fig. 3), the continuum arm requires only $K_{\text{rig}}/K_{\text{cont}} \approx 82\%$ of the input angle needed for the rigid arm. In conclusion, the continuum mechanism, with its compact mass distribution, provides superior attitude adjustment efficiency within the moving mass actuation framework, thereby reinforcing its pivotal role in the RGBlimp-Q design. Note that while the designed continuum arm shows higher compliance, further analysis is needed for generalized conclusions.

B. Motion Dynamics Modeling of RGBlimp-Q

In this section, we derive the translational and rotational dynamics model of the RGBlimp-Q, considering the continuum arm-based moving mass control. The RGBlimp-Q is modeled as a rigid-body system, subject to inertial forces and moments exerted by the moving mass within the robot, as well as aerodynamic forces and moments arising from the surrounding airflow, as illustrated in Fig. 4. The actuation of the system comprises a continuum arm serving as an internal movable mass m_a for moving mass control, along with a propeller generating forward thrust F .

The dynamics model is conceptualized as a system of two point masses, as shown in Fig. 4. The stationary mass, including wings and an envelope filled with helium, is denoted as m_0 , characterized by a constant displacement \mathbf{r}_0 with respect to CB. The internal movable mass, represented by a continuum arm with a gripper, is denoted as m_a , featuring a controllable displacement \mathbf{r}_a with respect to CB.

The coordinate frames and external forces are defined following the convention [54] and illustrated in Fig. 4. The position and orientation of the robot are defined with respect to the earth-fixed inertial frame $O-xyz$. Motion, including the translational and rotational velocities of the RGBlimp-Q, is referenced to a body-fixed frame $O_b-x_b y_b z_b$, with its origin O_b defined at CB. The velocity reference frame $O_b-x_v y_v z_v$ is established to model aerodynamics, with its O_b-x_v axis aligned with the direction of the translational velocity of the robot. The position vector $\mathbf{p} = [x, y, z]^T$ describes the displacement of the origin of the inertial frame O with respect to the origin of the body-fixed frame O_b . The Euler angles, including

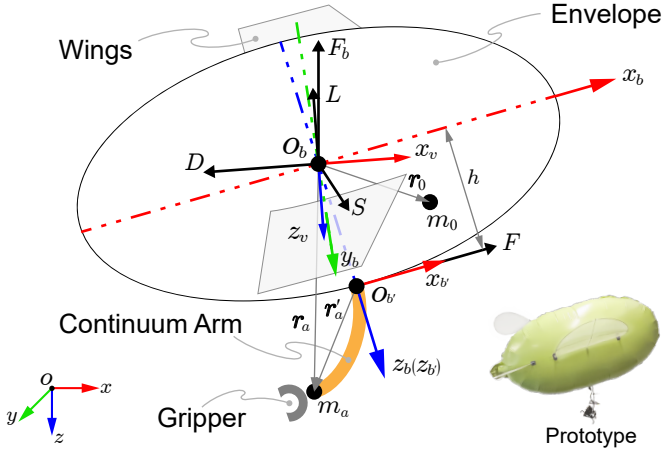


Fig. 4. Illustration of the RGBlimp-Q model, featuring a buoyant envelope, a continuum arm, and a pair of wings. The mass distribution includes the stationary mass m_0 and the internal movable mass m_a , with displacements r_0 and r_a relative to the center of buoyancy (CB), respectively. The continuum arm is equipped with a gripper, serving as an aerial robotic manipulator, as discussed in Section III-C. A snapshot of the RGBlimp-Q prototype is shown in the lower-right corner.

the roll angle $\phi \in (-\frac{\pi}{2}, \frac{\pi}{2})$, pitch angle $\theta \in (-\frac{\pi}{2}, \frac{\pi}{2})$, and yaw angle $\psi \in (-\pi, \pi)$, represent the orientation, denoted as $\boldsymbol{\eta} = [\phi, \theta, \psi]^T$. Let $\mathbf{v} = [\dot{x}, \dot{y}, \dot{z}]^T$ and $\boldsymbol{\omega} = [p, q, r]^T$ represent the translational velocity expressed in the inertial frame and rotational velocity expressed in the body-fixed frame, respectively. As commonly used in the literature [54], rotation from the body-fixed frame to the inertial frame follows the roll-pitch-yaw (RPY) sequence, i.e.,

$$\mathbf{R} = \mathbf{R}_z(\psi)\mathbf{R}_y(\theta)\mathbf{R}_x(\phi). \quad (4)$$

The relationship between the time derivative of any given vector \mathbf{c} expressed in the inertial frame $\dot{\mathbf{c}}^I$ and that expressed in the body-fixed frame $\dot{\mathbf{c}}^B$ follows¹

$$\dot{\mathbf{c}}^I = \mathbf{R}(\dot{\mathbf{c}}^B + \boldsymbol{\omega}^B \times \mathbf{c}^B). \quad (5)$$

To clarify the derivation, the motion dynamics model of the robot expresses all translational quantities in the inertial frame and all rotational quantities in the body-fixed frame. Where no ambiguity arises, the superscripts “I” and “B” are omitted, e.g., $\mathbf{v} = \mathbf{v}^I$ and $\boldsymbol{\omega} = \boldsymbol{\omega}^B$.

Then the kinematics of the RGBlimp-Q are described by

$$\dot{\mathbf{p}} = \mathbf{v}, \quad \dot{\boldsymbol{\eta}} = \mathbf{P}\boldsymbol{\omega}. \quad (6)$$

Here, the changing rate of the Euler angles $\dot{\boldsymbol{\eta}}$ and the rotational velocity $\boldsymbol{\omega}$ are related through the transformation matrix based on the RPY sequence, i.e.,

$$\mathbf{P} = \begin{bmatrix} 1 & \sin \phi \tan \theta & \cos \phi \tan \theta \\ 0 & \cos \phi & -\sin \phi \\ 0 & \sin \phi \sec \theta & \cos \phi \sec \theta \end{bmatrix}. \quad (7)$$

Based on Newton’s second law of motion, the translational motion expressed in the inertial frame is described as

$$\mathbf{F}_{\text{ext}} = m_0 (\dot{\mathbf{v}} + \mathbf{R}\mathbf{a}^B), \quad (8)$$

¹Here $\dot{\mathbf{R}} = \mathbf{R}\boldsymbol{\omega}^\times$ is used for derivation, where $\boldsymbol{\omega}^\times$ is the skew-symmetric matrix corresponding to $\boldsymbol{\omega}$.

where \mathbf{a}^B stands for the sum of Euler and centripetal acceleration expressed in the body-fixed frame, which is exerted by the point mass m_0 due to the displacement \mathbf{r}_0 , defined as

$$\mathbf{a}^B = \dot{\boldsymbol{\omega}} \times \mathbf{r}_0 + \boldsymbol{\omega} \times (\boldsymbol{\omega} \times \mathbf{r}_0). \quad (9)$$

The term \mathbf{F}_{ext} denotes the total external force acting on the stationary mass m_0 of the RGBlimp-Q, expressed in the inertial frame, calculated as

$$\mathbf{F}_{\text{ext}} = F\mathbf{R}\hat{\mathbf{i}} + (m_0g - F_b)\hat{\mathbf{k}} + \mathbf{R}\mathbf{F}_{\text{aero}}^B + \mathbf{f}_a. \quad (10)$$

Here, F represents the forward thrust force from the propeller, aligned with the x_b axis as shown in Fig. 4. The vectors $\hat{\mathbf{i}} = [1, 0, 0]^T$ and $\hat{\mathbf{k}} = [0, 0, 1]^T$ are unit vectors along the O_b - x_b and O - z axes, respectively. The scalar g is the gravitational acceleration. The scalar $F_b = \rho g V_{\text{He}}$ represents the buoyant lift, where ρ is the density of air and V_{He} is the volume of helium gas. The vector $\mathbf{F}_{\text{aero}}^B$ denotes the aerodynamic forces acting on the robot expressed in the body-fixed frame.

The term \mathbf{f}_a represents the total equivalent force acting on the stationary mass expressed in the inertial frame, exerted by the internal movable mass, which includes gravity and equivalent force, i.e.,

$$\mathbf{f}_a = m_a g \hat{\mathbf{k}} - m_a \dot{\mathbf{v}}_a. \quad (11)$$

Here, $\dot{\mathbf{v}}_a$ denotes the time derivative of the velocity of the internal movable mass m_a , expressed in the inertial frame, calculated as

$$\begin{aligned} \dot{\mathbf{v}}_a &= \frac{d\mathbf{v}_a}{dt} = \frac{d}{dt} \mathbf{R}(\mathbf{v}^B + \boldsymbol{\nu}_a + \boldsymbol{\omega} \times \mathbf{r}_a) \\ &= \dot{\mathbf{v}} + \mathbf{R}(\dot{\boldsymbol{\nu}}_a + 2\boldsymbol{\omega} \times \boldsymbol{\nu}_a + \dot{\boldsymbol{\omega}} \times \mathbf{r}_a + \boldsymbol{\omega} \times (\boldsymbol{\omega} \times \mathbf{r}_a)), \end{aligned} \quad (12)$$

where $\boldsymbol{\nu}_a = \dot{\mathbf{r}}_a$ represents the time derivative of the controllable displacement \mathbf{r}_a of the moving mass.

Based on Euler’s second axiom of motion, the rotational motion expressed in the inertial frame is described as

$$\mathbf{T} = \mathbf{J}\dot{\boldsymbol{\omega}} + \boldsymbol{\omega} \times (\mathbf{J}\boldsymbol{\omega}) + m_0 \mathbf{r}_0 \times \mathbf{R}^T \dot{\mathbf{v}}. \quad (13)$$

Here, the matrix $\mathbf{J} \in \mathbb{R}^{3 \times 3}$ represents the inertia matrix of the stationary mass about the origin of the body-fixed frame. The total external moment \mathbf{T} is calculated as

$$\mathbf{T} = Fh\hat{\mathbf{j}} + \mathbf{r}_0 \times m_0 g \mathbf{R}^T \hat{\mathbf{k}} + \mathbf{T}_{\text{aero}} + \mathbf{r}_a \times \mathbf{R}^T \mathbf{f}_a. \quad (14)$$

Here, the scalar h denotes the distance between the forward thrust F and the O_b - x_b axis, as depicted in Fig. 4. The vector $\hat{\mathbf{j}} = [0, 1, 0]^T$ represents the unit vector along the O_b - y_b axis. The vector \mathbf{T}_{aero} denotes the aerodynamic moment acting on the robot, expressed in the body-fixed frame.

Let vector $\mathbf{F}_a = m_a \dot{\mathbf{v}}_a = m_a \ddot{\mathbf{r}}_a$ represent the control input force exerted on the internal moving mass m_a in the body-fixed frame. Combining Eqs.(9)-(14), the motion dynamics of the RGBlimp-Q are expressed in terms of the control inputs including the forward thrust F and the moving mass actuation force \mathbf{F}_a as follows:

$$\mathbf{E} \begin{bmatrix} \dot{\mathbf{v}} \\ \dot{\boldsymbol{\omega}} \\ \dot{\mathbf{v}}_a \end{bmatrix} = \begin{bmatrix} \tilde{\mathbf{F}} \\ \tilde{\mathbf{T}} \\ \mathbf{0}_{3 \times 1} \end{bmatrix} + \mathbf{N} \begin{bmatrix} F \\ \mathbf{F}_a \end{bmatrix}, \quad (15)$$

where

$$\tilde{\mathbf{F}} = \mathbf{R}(\boldsymbol{\omega} \times \mathbf{l}_g) \times \boldsymbol{\omega} + ((m_0 + m_a)g - F_b)\hat{\mathbf{k}} + \mathbf{R}\mathbf{F}_{\text{aero}} + 2m_a\boldsymbol{\nu}_a \times \boldsymbol{\omega}, \quad (16)$$

$$\tilde{\mathbf{T}} = (\mathbf{J} - m_a(\mathbf{r}_a^\times)^2)\boldsymbol{\omega} \times \boldsymbol{\omega} + \mathbf{l}_g \times g\mathbf{R}^T\hat{\mathbf{k}} + \mathbf{T}_{\text{aero}} + 2m_a\mathbf{r}_a \times (\boldsymbol{\nu}_a \times \boldsymbol{\omega}), \quad (17)$$

$$\mathbf{E} = \begin{bmatrix} (m_0 + m_a)\mathbf{I} & -\mathbf{R}\mathbf{l}_g^\times & \mathbf{R} \\ \mathbf{l}_g^\times \mathbf{R}^T & \mathbf{J} - m_a(\mathbf{r}_a^\times)^2 & \mathbf{r}_a^\times \\ \mathbf{0}_3 & \mathbf{0}_3 & \mathbf{I} \end{bmatrix}, \quad (18)$$

$$\mathbf{N} = \begin{bmatrix} \mathbf{R}\hat{\mathbf{i}} & h\hat{\mathbf{j}} & \mathbf{0}_{1 \times 3} \\ \mathbf{0}_{3 \times 2} & \frac{1}{m_a}\mathbf{I} \end{bmatrix}^T. \quad (19)$$

Here, $\mathbf{l}_g = m_0\mathbf{r}_0 + m_a\mathbf{r}_a = (m_0 + m_a)\mathbf{r}_g$ where \mathbf{r}_g denotes the overall CG of the system of two point masses. $\mathbf{0}$ represents the zero vector or matrix. The matrix $\mathbf{I} \in \mathbb{R}^{3 \times 3}$ represents the identity matrix.

Additionally, the aerodynamics terms in Eqs. (16) and (17) need to be considered. Without loss of generality, we assume a windless environment, focusing on motion-induced aerodynamics. The transformation from the velocity reference frame $O_b-x_v y_v z_v$ to the body-fixed frame $O_b-x_b y_b z_b$ is expressed as

$$\mathbf{R}_v^b = \begin{bmatrix} \cos \alpha \cos \beta & -\cos \alpha \sin \beta & -\sin \alpha \\ \sin \beta & \cos \beta & 0 \\ \sin \alpha \cos \beta & -\sin \alpha \sin \beta & \cos \alpha \end{bmatrix}. \quad (20)$$

Here, the scalar $\alpha = \arctan(w/u)$ represents the angle of attack, and the scalar $\beta = \arcsin(v/V)$ denotes the sideslip angle, where the velocity magnitude $V = \|\mathbf{v}\|$ and the velocity expressed in the body-fixed frame $\mathbf{v}^B = \mathbf{R}^T \mathbf{v} = [u, v, w]^T$.

As illustrated in Fig. 4, the aerodynamic forces, including the drag force D , the side force S , and the lift force L , are defined in the velocity reference frame. Similarly, the aerodynamic moments comprise the roll moment M_x , the pitch moment M_y , and the yaw moment M_z . The aerodynamic forces and moments are described as

$$\mathbf{F}_{\text{aero}} = \mathbf{R}_v^b[-D, S, -L]^T, \quad \mathbf{T}_{\text{aero}} = \mathbf{R}_v^b[M_x, M_y, M_z]^T, \quad (21)$$

which are modeled as $[D, S, L]^T = \frac{1}{2}\rho V^2 A [C_D, C_S, C_L]^T$ and $[M_x, M_y, M_z]^T = \frac{1}{2}\rho V^2 A [C_{M_x}, C_{M_y}, C_{M_z}]^T + [K_x, K_y, K_z]\boldsymbol{\omega}$, where A is the aerodynamic reference area. The terms with ‘‘C’’ and ‘‘K’’ denote the constant aerodynamic and damping coefficients, respectively, as experimentally identified in Section IV-C.

C. Moving Mass Actuation via Continuum Mechanism

As an essential design feature, the continuum mechanism implements moving mass actuation in the RGBlimp-Q. This section introduces the details and kinematics of the continuum arm without twist, based on the assumption of constant curvature (CC). Furthermore, we simplify the continuum arm with a lightweight and fixed-length elastic backbone (the central axis), thus a point mass m_a on the end of the arm is considered, which is moving on a manifold with 2 DoF.

Figure 5 illustrates the CC model, where the continuum arm is approximated as a continuous segment with a curvature constant in space but varying in time. The base frame of the continuum arm $O_{b'}-x_{b'} y_{b'} z_{b'}$ has the same orientation as the

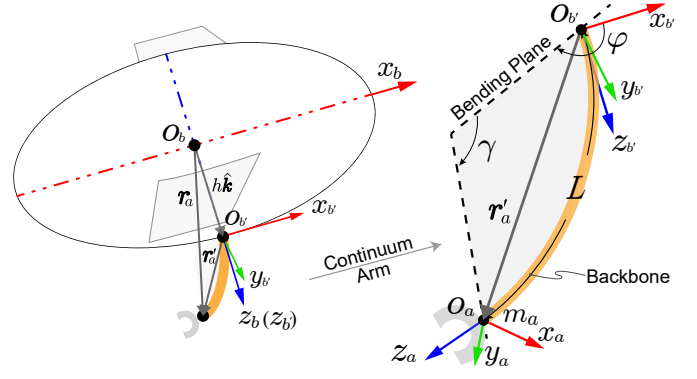


Fig. 5. The geometric illustration of a continuum arm’s spatial motion shows the arm bending in a plane, defined by the curvature angle γ , the bending direction φ , and reference frames: the base frame $O_{b'}-x_{b'} y_{b'} z_{b'}$ and the end-effector frame $O_a-x_a y_a z_a$.

body-fixed frame $O_b-x_b y_b z_b$, but translated along O_b-z_b axis with a distance h , as shown in Fig. 5. The end-effector frame of the continuum arm $O_a-x_a y_a z_a$ is established at the end of the continuum arm. Under the CC assumption, the kinematic homogeneous transformation matrix $\mathbf{C}_b^t \in \text{SE}(3)$ maps arm $O_{b'}-x_{b'} y_{b'} z_{b'}$ into $O_a-x_a y_a z_a$, given by

$$\mathbf{C}_b^t(\gamma, \varphi) = \mathbf{R}_z(\varphi) \begin{bmatrix} \mathbf{R}_x(\gamma) & \frac{L}{\gamma} \begin{bmatrix} \cos \gamma - 1 \\ \sin \gamma \\ 0 \end{bmatrix} \\ 0 & 1 \end{bmatrix} \mathbf{R}_z(-\varphi). \quad (22)$$

Here, L is the constant length of the continuum arm backbone. The angle $\varphi \in [0, 2\pi)$ and $\gamma \in [0, \pi/2]$ stand for the direction of bending and the angle of curvature, respectively, as shown in Fig. 5. The matrices $\mathbf{R}_x, \mathbf{R}_z \in \text{SO}(3)$ represent the rotation matrices about the $x_{b'}$ and $z_{b'}$ axes, respectively.

We examine the translation vector from $O_{b'}-x_{b'} y_{b'} z_{b'}$ to $O_a-x_a y_a z_a$, denoted as \mathbf{r}'_a . Derived from the transformation matrix (22), the expression for \mathbf{r}'_a is given by

$$\mathbf{r}'_a(\varphi, \gamma) = \frac{L}{\gamma} \begin{bmatrix} \cos \varphi(1 - \cos \gamma) \\ \sin \varphi(1 - \cos \gamma) \\ \sin \gamma \end{bmatrix}. \quad (23)$$

As shown in Fig. 4, the translation vector \mathbf{r}'_a plays a crucial role in the moving mass control, which determines the controllable displacement \mathbf{r}_a , i.e., $\mathbf{r}_a = [0, 0, h]^T + \mathbf{r}'_a$.

The configuration $[\gamma, \varphi]^T$ represents a standard parametrization commonly used in continuum robot studies [43], [49]. To address the inherent limitations of this approach, Santina and Rus proposed a novel q -parametrization for continuum arms, which are actuated by four evenly distributed cables and have no twist. This parametrization is defined as linear combinations of the four cable lengths [50]. For a lightweight-oriented design that also facilitates spatial motion, we consider a configuration with three cables—the minimum required for a single-segment cable-driven spatial continuum. Furthermore, we derive the q -parametrization for this three-cable configuration, establishing its kinematic mapping relationship.

Figure 6 illustrates the q -parametrization of the three-cable-driven continuum arm, featuring three evenly distributed cables l_1, l_2 , and l_3 aligned parallel to the backbone in the bending plane of the continuum arm. These cables share the same

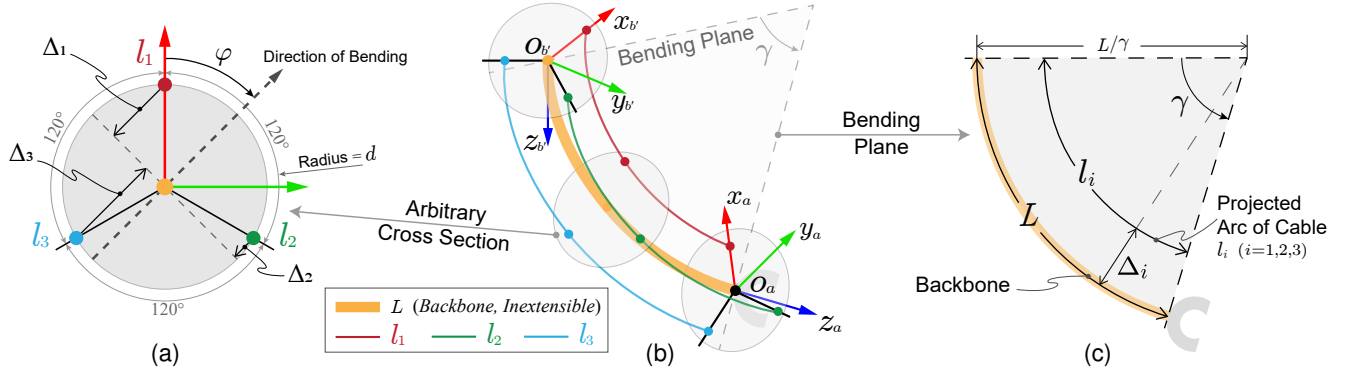


Fig. 6. Illustration of the q -parametrization of the three-cable-based continuum arm. The parameters $q = [\delta_x, \delta_y]^T \in \mathbb{R}^2$ are defined as a linear combination of the lengths of the three evenly distributed cables (l_1, l_2, l_3). (a) depicts the geometric relation in arbitrary cross section, where the cables are connected without twist and are equidistant, each at a distance d from the center. (b) illustrates the entire continuum body deformed by the three cables. (c) shows the bending plane from a perpendicular view, visually illustrating the projected arc of any cable l_i , ($i=1, 2, 3$) at corresponding projection distance Δ_i , as in (a).

curvature as the backbone, maintaining a constant distance d from the center in an arbitrary cross section of the continuum arm, as shown in the right plot of Fig. 6. Trigonometric considerations allow us to derive the projection distances on the bending plane Δ_i ($i=1, 2, 3$) of the constant distance d for each cable, i.e.,

$$\Delta_1 = +d \cos \varphi, \quad \Delta_{2,3} = -d \sin\left(\frac{\pi}{6} \mp \varphi\right). \quad (24)$$

Further, the length of cable l_i , ($i=1, 2, 3$) with the projection distance Δ_i , as shown in Fig. 6, is calculated by

$$l_i = \gamma\left(\frac{L}{\gamma} - \Delta_i\right) = L - \gamma\Delta_i, \quad (i=1, 2, 3). \quad (25)$$

Combining Eqs. (24) and (25) yields the lengths of the three cables as functions of γ and φ , i.e.,

$$\begin{aligned} l_1(\gamma, \varphi) &= L - d\gamma \cos \varphi, \\ l_2(\gamma, \varphi) &= L + d\gamma \sin\left(\frac{\pi}{6} - \varphi\right), \\ l_3(\gamma, \varphi) &= L + d\gamma \sin\left(\frac{\pi}{6} + \varphi\right). \end{aligned} \quad (26)$$

Furthermore, we define the new state configuration as linear combinations of the three cable lengths, as expressed through the q -parametrization, i.e.,

$$\begin{aligned} \delta_x &= \frac{1}{3}(l_2 + l_3 - 2l_1) = d\gamma \cos \phi, \\ \delta_y &= \frac{\sqrt{3}}{3}(l_3 - l_2) = d\gamma \sin \phi, \\ \delta &= \sqrt{\delta_x^2 + \delta_y^2} = d\gamma \end{aligned} \quad (27)$$

Let $q = [\delta_x, \delta_y]^T \in \mathbb{R}^2$ represent the continuum configuration in q -parametrization, describing the bending degree in the $x_{b'}$ and $y_{b'}$ directions, respectively. The mapping from the q -parametrization to the angle parametrization is described as

$$\varphi = \arccos\left(\frac{\delta_x}{\delta}\right) = \arcsin\left(\frac{\delta_y}{\delta}\right), \quad \gamma = \frac{\delta}{d}. \quad (28)$$

Let the velocity in q -parametrization serve as the control input, denoted as $\dot{\delta}_x$ and $\dot{\delta}_y$. Such input is well-suited for a cable-driven continuum arm, discussed in detail in Section III-A. Combining Eqs. (23) and (28), the translation vector r'_a in the q -parametrization is given by

$$r'_a(\delta_x, \delta_y) = \frac{Ld}{\delta^2} \begin{bmatrix} \delta_x(1 - \cos \frac{\delta}{d}) \\ \delta_y(1 - \cos \frac{\delta}{d}) \\ \delta \sin \frac{\delta}{d} \end{bmatrix}. \quad (29)$$

Therefore, the time derivative of the displacement vector $r_a = [0, 0, h]^T + r'_a$ is determined as

$$\dot{r}_a = \frac{\partial r'_a}{\partial(\delta_x, \delta_y)} \begin{bmatrix} \dot{\delta}_x \\ \dot{\delta}_y \end{bmatrix}, \quad (30)$$

where $\partial r'_a / \partial(\delta_x, \delta_y) \in \mathbb{R}^{3 \times 2}$ denotes the Jacobian matrix of the RHS of Eq. (30).

D. Full Dynamic Model of RGBlimp-Q

Combining the motion dynamics (16) and the kinematics of the continuum arm (30), we derive the full dynamic model of the RGBlimp-Q, expressed in terms of the system states p, η, v, ω, r_a and the control inputs $F, \dot{\delta}_x, \dot{\delta}_y$, i.e.,

$$\begin{bmatrix} \dot{p} \\ \dot{\eta} \\ \dot{r}_a \\ \dot{v} \\ \dot{\omega} \end{bmatrix} = \begin{bmatrix} v \\ P\omega \\ \mathbf{0}_{3 \times 1} \\ A \begin{bmatrix} \tilde{f} \\ \tilde{t} \end{bmatrix} \end{bmatrix} + B \begin{bmatrix} F \\ \dot{\delta}_x \\ \dot{\delta}_y \end{bmatrix}, \quad (31)$$

where

$$\tilde{f} = R(\omega \times l_g) \times \omega + ((m_0 + m_a)g - F_b)\hat{k} + RF_{\text{aero}}, \quad (32)$$

$$\tilde{t} = (J - m_a(r_a^\times)^2)\omega \times \omega + l_g \times gR^T\hat{k} + T_{\text{aero}}, \quad (33)$$

$$A = \begin{bmatrix} (m_0 + m_a)\mathbf{I} & -Rl_g^\times \\ l_g^\times R^T & J - m_a(r_a^\times)^2 \end{bmatrix}^{-1}, \quad (34)$$

$$B = \begin{bmatrix} \mathbf{0}_{6 \times 4} & & & \\ & \mathbf{0}_{3 \times 1} & \mathbf{I} & \\ & A \begin{bmatrix} \hat{i} \\ h\hat{j} \end{bmatrix} & -2\omega^\times & \\ & & -2r_a^\times \omega^\times & \end{bmatrix} \begin{bmatrix} 1 & \mathbf{0}_{1 \times 2} \\ \mathbf{0}_{3 \times 1} & \frac{\partial r'_a}{\partial(\delta_x, \delta_y)} \end{bmatrix}. \quad (35)$$

Here, the allocation matrix A is always invertible (see Appendix A for proof), ensuring that A^{-1} is always well-defined. The inertial matrix $J - m_a(r_a^\times)^2$ in Eq. (34) represents the effective rotational inertia of the entire system, including both the stationary mass m_0 and the moving mass m_a , i.e.,

$$\begin{aligned} J_{\text{eff}} &= J - m_a(r_a^\times)^2 \\ &= J + m_a(\|r_a\|^2 \mathbf{I} - r_a r_a^T). \end{aligned} \quad (36)$$

The design of RGBlimp-Q ensures that $\mathbf{r}_a \neq \mathbf{0}$ and $\mathbf{J} \succ 0$, which guarantees that $\det(\mathbf{J}_{\text{eff}}) > 0$. This ensures that the dynamics described by Eq. (31) remain well-posed (i.e., avoiding ill-conditioning), and that rotational sensitivity remains bounded. For example, the roll angular acceleration $\ddot{\phi} = \tau_x / J_{xx}$ remains finite as long as $J_{xx} > 0$, where τ_x denotes the torque around the x -axis.

III. CONTINUUM ARM SYSTEM

In this section, we present the design of a decoupled, cable-driven continuum arm with an end-effector claw, specifically developed to support the proposed moving-mass-based attitude adjustment of RGBlimp-Q, see Fig. 7.

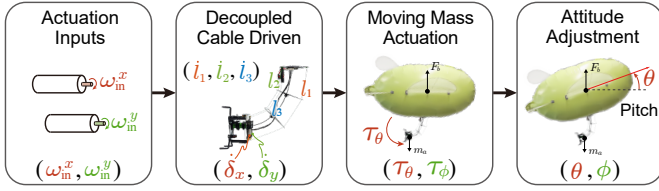


Fig. 7. The schematic diagram illustrates the proposed decoupled mechanism, which enables decoupled cable-driven control of the continuum arm and facilitates moving mass actuation for attitude adjustment of RGBlimp-Q. The decoupled mechanism enables the mechanism-level decoupled control of the continuum arm for 2-DoF spatial motion using two actuators. Specifically, a compound gear train is designed to coordinate the adjustment of three cables under continuum constraints, thereby realizing the 2-DoF spatial motion required for moving mass actuation. This motion facilitates attitude adjustment of RGBlimp-Q in both pitch θ and roll ϕ directions.

The mechanism enables decoupled control of the continuum arm to achieve 2-DoF spatial motion using only two actuators. This design eliminates the need for redundant actuators, thereby significantly reducing both system weight and energy consumption—critical considerations for payload-constrained robotic blimp platforms.

A. Mechanically Decoupled Cable-Driven Design

In our design, we consider the continuum arm without twist under the CC assumption, as discussed in Section II-C and illustrated in Fig. 6, where the cables are treated as the driving cables. To achieve spatial motion of the continuum arm, a minimum of three cables is required. These cables are constrained by the backbone, resulting in a two-degree-of-freedom motion described in terms of either (γ, φ) or (δ_x, δ_y) . In the literature [41]–[43], these cables are typically controlled by independent actuators (motors) within specific constraints. However, such redundancy in motors leads to increased inefficiency in load handling, a concern that is particularly pertinent in the design of miniature aircraft such as the RGBlimp-Q. To mitigate this inefficiency, we utilize a compound gear train mechanism to achieve decoupling for the cable-driven continuum arm. This approach ensures that the two-degree-of-freedom motion of the robot is independently controlled by two corresponding actuators.

Let's reconsider the relationship between three cable lengths (l_1, l_2, l_3) and the q -parametrization configuration (δ_x, δ_y) .

Combining Eqs. (26) and (27), we derive the lengths of the three cables as functions of δ_x and δ_y , i.e.,

$$\begin{bmatrix} l_1 \\ l_2 \\ l_3 \end{bmatrix} = \begin{bmatrix} -1 & 0 \\ 1 & -\frac{\sqrt{3}}{2} \\ 1 & \frac{\sqrt{3}}{2} \end{bmatrix} \begin{bmatrix} \delta_x \\ \delta_y \end{bmatrix}. \quad (37)$$

These equations reveal that the lengths of the three cables are kinematically constrained by a linear relationship, i.e., $l_1 + l_2 + l_3 = 0$. Further, it is observed that the length l_1 is independent of δ_y but decreases with δ_x . Meanwhile, l_2 and l_3 increase with $\frac{1}{2}\delta_x$. The length l_2 decreases with $\frac{\sqrt{3}}{2}\delta_y$, while l_3 increases with $\frac{\sqrt{3}}{2}\delta_y$.

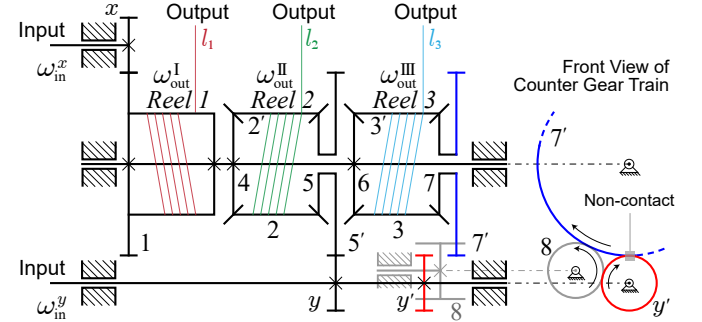


Fig. 8. Representation of the proposed compound-gear-train-based decoupling mechanism. The design ensures independent control for the 2 DoF of the continuum arm by two actuators accordingly. The three cables are wound at each of three outputting reels, including differential-based reels 2 and 3, and the fixed-axis reel 1 with an opposite winding direction. The left part of the figure shows the main structure of the mechanism in the side view. The right part depicted the front view of the counter gear, i.e., gear 8, whose rotating axis is in a different plane. Note that the gear 7' (blue) and 8 (red) are not engaged, as shown in the side view.

Based on Eq. (37), we propose the mechanism of a compound gear train for decoupled cable driving, as shown in Fig. 8. The mechanism uses two actuators for decoupled inputs, yielding three rotary motions for winding the three cables under the constraint in Eq. (37) accordingly. The inputs and outputs of the mechanism are defined as the rotational speeds of the two actuators and the three reels, respectively, denoted as $(\omega_{\text{in}}^x, \omega_{\text{in}}^y)$ and $(\omega_{\text{out}}^{\text{I}}, \omega_{\text{out}}^{\text{II}}, \omega_{\text{out}}^{\text{III}})$. Specifically, reel 1 is directly affixed to a shaft, i.e., the fixed-axis reel, while reel 2 and reel 3 are made of differential gear trains, i.e., differential-based reels. The setup includes seven spur gears ($x, y, y', 1, 5', 7', 8$) and eight bevel gears ($2, 2', 3, 3', 4, 5, 6, 7$). To determine the overall drive ratio R of the compound gear train, we examine the rotational speeds ω and tooth numbers n of each gear. Beginning with the fixed-axis gear train segment, we compute the rotational speed of reel 1 as

$$\omega_{\text{out}}^{\text{I}} = R_x^1 \omega_{\text{in}}^x = -\frac{n_x}{n_1} \omega_{\text{in}}^x. \quad (38)$$

Here, R_x^1 represents the drive ratio from gear x to gear 1, with the negative sign indicating the opposite direction of rotation. In addition, gear 4 and gear 6 are fixed on the same shaft with gear 1, resulting in $\omega_4 = \omega_6 = \omega_1$. Similarly, we obtain

$$\omega_5 = \omega_{5'} = -\frac{n_y}{n_{5'}} \omega_{\text{in}}^y, \quad \omega_7 = \omega_{7'} = \frac{n_8}{n_{7'}} \frac{n_{y'}}{n_8} \omega_{\text{in}}^y. \quad (39)$$

The tooth numbers of bevel gears in the differential gear train are designed the same, i.e., $n_4 = n_5 = n_6 = n_7$. Thus, the rotational speeds of reels 2 and 3 are calculated as

$$\omega_{\text{out}}^{\text{II}} = \frac{1}{2}(\omega_4 + \omega_5), \quad \omega_{\text{out}}^{\text{III}} = \frac{1}{2}(\omega_6 + \omega_7). \quad (40)$$

Combining Eqs. (38), (39) and (40), we obtain the rotational speeds of reels 2 and 3 as

$$\omega_{\text{out}}^{\text{II}} = -\frac{1}{2} \frac{n_x}{n_1} \omega_{\text{in}}^x - \frac{1}{2} \frac{n_y}{n_{5'}} \omega_{\text{in}}^y, \quad \omega_{\text{out}}^{\text{III}} = -\frac{1}{2} \frac{n_x}{n_1} \omega_{\text{in}}^x + \frac{1}{2} \frac{n_y}{n_{7'}} \omega_{\text{in}}^y.$$

Here, we selected two different sets of tooth numbers for spur gears, i.e., $n_x = n_y = n_{y'} = n_8$ and $n_1 = n_{5'} = n_{7'}$. Combining Eq. (45) with $k = n_x/n_1 = n_y/n_{5'} = n_{y'}/n_{7'}$, thus

$$\omega_{\text{out}}^{\text{I}} = -k\omega_{\text{in}}^x, \quad \omega_{\text{out}}^{\text{II}} = -\frac{1}{2}k(\omega_{\text{in}}^x + \omega_{\text{in}}^y), \quad \omega_{\text{out}}^{\text{III}} = -\frac{1}{2}k(\omega_{\text{in}}^x - \omega_{\text{in}}^y).$$

Considering that cable l_1 is wound in the opposite direction to l_2 and l_3 , and the radii of the reels are designed the same, denoted as r_{reel} , the velocities of the cables are calculated as

$$\begin{bmatrix} \dot{l}_1 \\ \dot{l}_2 \\ \dot{l}_3 \end{bmatrix} = \begin{bmatrix} -1 & 0 \\ 1 & -\frac{\sqrt{3}}{2} \\ 1 & \frac{\sqrt{3}}{2} \end{bmatrix} \begin{bmatrix} kr_{\text{reel}}\omega_{\text{in}}^x \\ \frac{\sqrt{3}}{3}kr_{\text{reel}}\omega_{\text{in}}^y \end{bmatrix}. \quad (41)$$

Comparing Eqs. (37) and (41), we find

$$\dot{\delta}_x = kr_{\text{reel}}\omega_{\text{in}}^x, \quad \dot{\delta}_y = \frac{\sqrt{3}}{3}kr_{\text{reel}}\omega_{\text{in}}^y. \quad (42)$$

By considering $(\omega_{\text{in}}^x, \omega_{\text{in}}^y)$ as inputs, the decoupled cable-driven mechanism facilitates independent control of the 2-DoF continuum arm using two actuators, thereby mitigating the complexity of controlling the three cables.

B. Moving-Mass-Based Attitude Control

The decoupled cable-driven mechanism enables independent control of the continuum-based moving mass in 2 DoF through inputs $(\omega_{\text{in}}^x, \omega_{\text{in}}^y)$, thereby adjusting attitude in pitch (θ) and roll (ϕ). In this section, we propose an attitude controller for the RGBlimp-Q based on a classic PID feedback framework and demonstrate its stability. This controller is implemented to demonstrate the inherent advantages of the novel continuum-based moving mass actuation mechanism design in enabling effective attitude adjustment and efficient power utilization, as illustrated by experiments in Section V.

Two IMUs are employed as feedback sensors, mounted at both ends of the continuum arm, specifically the base frame $O_{b'}-x_{b'}y_{b'}z_{b'}$ and the end-effector frame $O_a-x_a y_a z_a$ of the continuum arm. Leveraging extended Kalman filters (EKF) and the kinematics of the continuum arm Eqs. (28)-(30), these sensors provide crucial information regarding the robot's attitude and the arm configuration. Figure 9 illustrates the schematic of the feedback controller.

Overall, the control objectives encompass tracking the desired configuration of the continuum arm and maintaining the desired flight attitude. To achieve this, the controller is designed into an inner loop and an outer loop, aligning with these two objectives, respectively. The inner-loop controller governs the movement of the two motors controlling the continuum arm, thereby managing the tracking error in its configuration (δ_x, δ_y) . More importantly, the outer-loop controller adjusts the robot's attitude by utilizing the gravitational

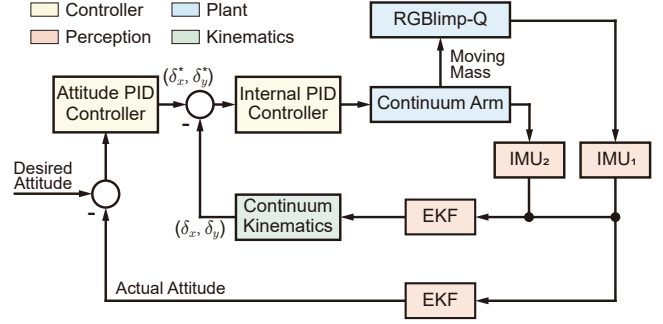


Fig. 9. Control schematic of the dual-loop PID. The internal controller regulates the continuum arm configuration in the q -parametrization, i.e., (δ_x, δ_y) . The attitude controller adjusts the orientation of RGBlimp-Q, specifically the roll, pitch, and yaw angles, utilizing both the gravitational moment of the moving mass and the aerodynamic moments.

moment induced by the moving mass for the pitch angle θ and the roll angle ϕ , as well as the aerodynamic yaw moment generated by airflow for the yaw angle ψ .

For clarity, we analyze pitch attitude tracking stability under moving mass actuation with δ_x as active control input and δ_y fixed. The pitch dynamics of RGBlimp-Q are represented by

$$J_{yy}^{\text{eff}}(\delta_x) \ddot{\theta} = \tau_{\theta}(\delta_x) - D_{\theta} \dot{\theta} + \Delta_{\theta}. \quad (43)$$

Here, $\tau_{\theta} = m_a g r_{a,x}$ is the gravitational moment generated by the continuum-based moving mass, $D_{\theta} > 0$ represents the pitch damping coefficient, and Δ_{θ} is a bounded disturbance with $|\Delta_{\theta}| \leq \rho_{\theta}$, where $\rho_{\theta} > 0$ denotes the upper bound of the pitch disturbance. $J_{yy}^{\text{eff}} = J_{yy} + m_a (r_{a,x}^2 + r_{a,z}^2)$ denotes the corresponding diagonal component of the effective rotational inertia tensor $\mathbf{J}_{\text{eff}} = \mathbf{J} + m_a (\|\mathbf{r}_a\|^2 \mathbf{I} - \mathbf{r}_a \mathbf{r}_a^T)$, where $r_{a,x} = \frac{Ld}{\delta_x} (1 - \cos \frac{\delta_x}{d})$ and $r_{a,z} = \frac{Ld}{\delta_x} \sin \frac{\delta_x}{d}$ from the kinematics of the continuum arm. For simplicity, we assume $\delta_x \ll d$, thus

$$r_{a,x} \approx \frac{L\delta_x}{2d}, \quad r_{a,z} \approx h + L. \quad (44)$$

The effective inertia is simplified as

$$J_{yy}^{\text{eff}}(\delta_x) \approx J_{yy} + m_a \left(\frac{L^2 \delta_x^2}{4d^2} + (h + L)^2 \right), \quad (45)$$

with $j_{yy}^{\text{eff}} \approx \frac{m_a L^2}{2d^2} \delta_x \dot{\delta}_x$ and $\tau_{\theta} \approx -\frac{m_a g L}{2d} \delta_x$.

Given the desired pitch angle θ^* , the outer-loop pitch attitude control law is $\delta_x = -k_p e_{\theta} - k_d \dot{e}_{\theta}$, where $k_p, k_d > 0$ are the control gains, $e_{\theta} = \theta - \theta^*$ represents the tracking error, and $\dot{e}_{\theta} = \dot{\theta}$. Considering time-varying inertia $J_{yy}^{\text{eff}}(\delta_x)$ and disturbances Δ_{θ} , we define the following quadratic function as the Lyapunov function for stability analysis, i.e.,

$$V(x) = \frac{1}{2} J_{yy}^{\text{eff}} \dot{e}_{\theta}^2 + \frac{1}{2} k_p e_{\theta}^2 + \frac{\lambda}{4} \delta_x^2, \quad (46)$$

where $\frac{\lambda}{4} \delta_x^2$ represents control energy with tunable parameter $\lambda > 0$. Combining both the pitch dynamics (43) and the control law, the time derivative \dot{V} is calculated and simplified as

$$\begin{aligned} \dot{V} = & - \left(D_{\theta} + \frac{m_a g L k_d}{2d} \right) \dot{e}_{\theta}^2 - \frac{\lambda k_p}{2} e_{\theta}^2 - \frac{\lambda k_d}{2} \dot{e}_{\theta}^2 + \\ & \frac{1}{2} \left(\frac{m_a L^2}{d^2} \delta_x \dot{\delta}_x \dot{e}_{\theta}^2 - \lambda k_p e_{\theta} \dot{e}_{\theta} \right) + \dot{e}_{\theta} \Delta_{\theta}. \end{aligned} \quad (47)$$

Applying Young's inequality to the disturbance $\dot{e}_{\theta} \Delta_{\theta}$ yields

$$\dot{e}_{\theta} \Delta_{\theta} \leq \frac{\epsilon}{2} \dot{e}_{\theta}^2 + \frac{\rho_{\theta}^2}{2\epsilon}, \quad (48)$$

where $\rho_\theta > 0$ indicates the maximum pitch disturbance, and the design parameter $\epsilon > 0$ adjusts the trade-off between error and disturbance. Meanwhile, the cross terms $\frac{1}{2} \left((m_a L^2 / d^2) \delta_x \dot{\delta}_x \dot{e}_\theta^2 - \lambda k_p e_\theta \dot{e}_\theta \right)$ are eliminated by imposing the gain condition

$$\lambda > \frac{m_a L^2}{d^2} \cdot \frac{\max |\delta_x \dot{\delta}_x|}{k_p}, \quad (49)$$

which allows the Lyapunov function derivative to be upper bounded by

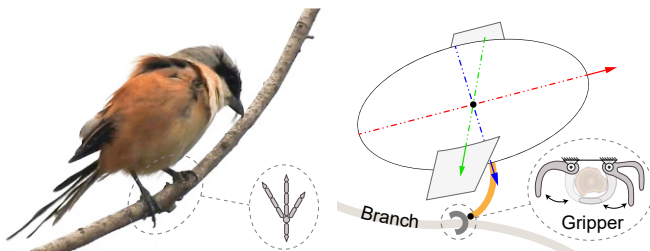
$$\dot{V} \leq -a \dot{e}_\theta^2 - b e_\theta^2 + \frac{\rho_\theta^2}{2\epsilon}, \quad (50)$$

where $a = D_\theta + \frac{m_a g L k_d}{2d} + \frac{\lambda k_d}{2} - \frac{\epsilon}{2}$ and $b = \frac{\lambda k_p}{2}$. Thus, gains k_p , k_d , and λ satisfying $D_\theta + \frac{m_a g L k_d}{2d} + \frac{\lambda k_d}{2} > \frac{\rho_\theta}{2}$ guarantee the negative definiteness of the Lyapunov function derivative \dot{V} . For disturbance-free flight ($\rho_\theta = 0$), the inequality $\dot{V} \leq -a \dot{e}_\theta^2 - b e_\theta^2$ holds, establishing global asymptotic stability of the pitching dynamics. With bounded disturbances ($\rho_\theta \neq 0$), the pitching tracking system is uniformly ultimately bounded (UUB) with a convergence radius $\|e_\theta\| \leq |\rho_\theta| / \sqrt{\epsilon \lambda k_p}$, where ϵ is the decay rate coefficient in the Lyapunov analysis.

Furthermore, real-world experiments with the RGBlimp-Q prototype presented in Section V validate the theoretical analysis, demonstrating stable flight and robust disturbance rejection by the proposed controller.

C. A Bionic Bird's Claw for Resisting Wind

With their claws, birds effortlessly grasp and perch on trees, especially in windy conditions, as illustrated in Fig. 10. In contrast, current robotic blimps lack such an adaptive mechanism to withstand wind disturbances.



(a) Bird perching and anchoring. (b) Bird-inspired perching strategy.

Fig. 10. The gripper is a bird-inspired robotic effector mounted at the end of the continuum arm, which enables robotic blimps to catch objects for resting or resisting wind. (a) Birds use their claws, usually anisodactyl, to grasp branch securely and to anchor the body in a windy environment [35]. (b) The RGBlimp-Q adopts the same strategy to resist environmental wind with its gripper open for standing and closed for holding a branch.

Although robotic blimps feature durability, safety, and low noise levels compared to other aerial robots, they suffer from the long-standing challenge of wind disturbance, limiting their outdoor applications. To address this limitation, we propose a bio-inspired claw mechanism integrated with the continuum arm, mimicking behaviors of avian legs and claws.

The bio-inspired claw is a lightweight robotic gripper mounted at the end of the continuum arm, mimicking the anisodactyl structure of a bird's foot, with the first toe pointing backwards and the remaining toes facing forward. This configuration provides a wider grasping area when the claw is

open and ensures a reliable grasp when closed, thus enabling efficient aerial manipulation. Additionally, the buoyancy and gravity of the RGBlimp-Q ensure that its attitude remains stable whether the claw is open or closed.

Furthermore, the integration of the continuum arm with the end-effector claw offers complementary benefits. Specifically, the concentrated weight at the arm's end facilitates moving mass actuation. The inherent flexibility and passive compliance of the continuum arm further enhance the efficiency of aerial manipulation tasks.

IV. PROTOTYPE AND EXPERIMENTAL SETUP

In this section, we provide a detailed description of the prototype and experimental setup. The moving-mass-based prototype's experimental flights are described in Section V.

A. Continuum Arm Prototype

Following the design of the continuum arm, we have successfully developed a prototype, as shown in Fig. 11. The computer-aided design (CAD) models have been made available as open source on GitHub (<https://rgblimp.github.io>). The weight of the continuum arm is 81.79 g, excluding batteries, and it has a total length of 0.4 m with a backbone measuring 0.3 m made of nickel-titanium alloy.

The continuum arm comprises four main components, arranged from top to bottom, as illustrated in Fig. 11(a). At the top plate, a propeller and an IMU are mounted, serving propulsion and sensing functions, respectively. This plate also acts as a connector to the envelope of RGBlimp-Q. Below, the continuum body consists of three driven cables, two support plates, and the backbone. Meanwhile, the driven cables are constrained by the support plates to maintain a constant distance of $d = 40$ mm (as shown in Fig. 6) from the backbone while preventing twisting, thereby ensuring that the arm's motion conforms to the CC assumption. The driving box houses the gearbox for the decoupled cable-driven mechanism, two motors, a control unit, and another IMU. The decoupled mechanism is detailed in the CAD model, featuring one fixed-axis reel and two differential-based reels. Finally, the bionic gripper is affixed to the bottom of the continuum arm for standing or grasping objects, as illustrated in Fig. 11(d). It is worth noting that the driving cables wind in opposite directions between the fixed-axis reel and the two differential-based reels. Furthermore, these cables are guided from a horizontal to a vertical orientation through Teflon tubes, facilitating the movement of the continuum arm.

The propeller, with a diameter of 31 mm, is powered by a brushless DC (BLDC) motor *SE0802-KV19000* and an electronic speed controller (ESC) to regulate its speed effectively. Driving the system is a low-cost microcontroller *ESP32*, leveraging the *rosserial_arduino* library to establish a *Robot Operating System* (ROS) node, facilitating wireless network communication with a host computer.

B. RGBlimp-Q Prototype

A prototype of the RGBlimp-Q is developed, combining the continuum arm (acting as the moving mass m_a) and the

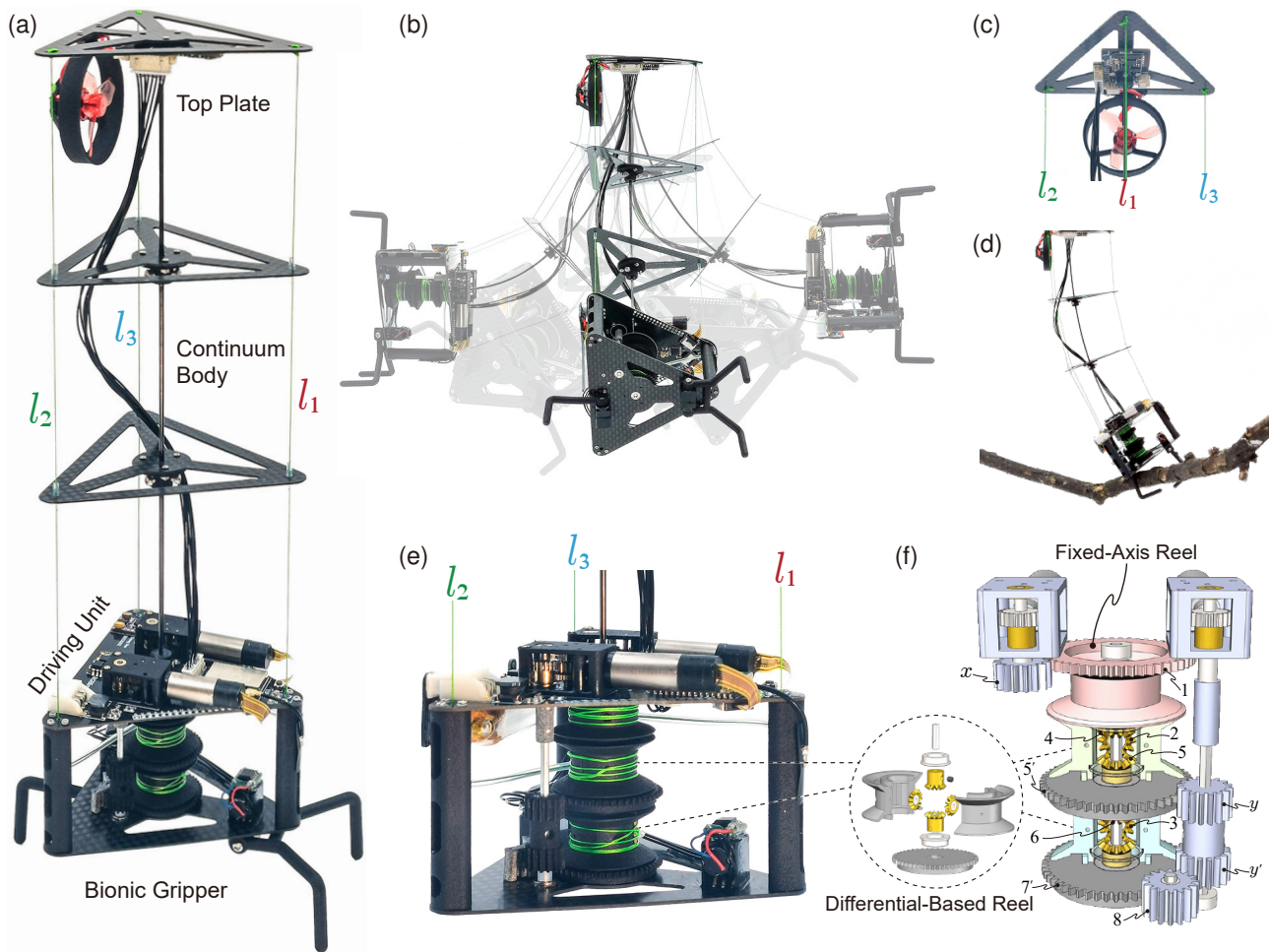


Fig. 11. Prototype of the continuum arm. (a) Four main parts make up the continuum arm, including the top plate, the continuum body, the driving unit, and the bionic gripper. (b) The spatial motion of the continuum arm is 2 DoF, which is constrained by the continuum body and driven by three cables. (c) The top plate includes a propeller and an IMU, whose circuit board and carbon fiber plate are connected to the driving unit by wires and cables, respectively. (d) The bionic gripper of the prototype holds a branch for resting or resisting wind. (e) The driving unit controls the continuum arm, the propeller and the bionic gripper based on sensor feedback, accounting for the main weight, i.e., ~ 65 g (80% total). (f) The gear box is composed of one fixed-axis reel, two differential-based reels, two motors with worm gear reducers, and gears of the same tooth number as designed in Section III-A.

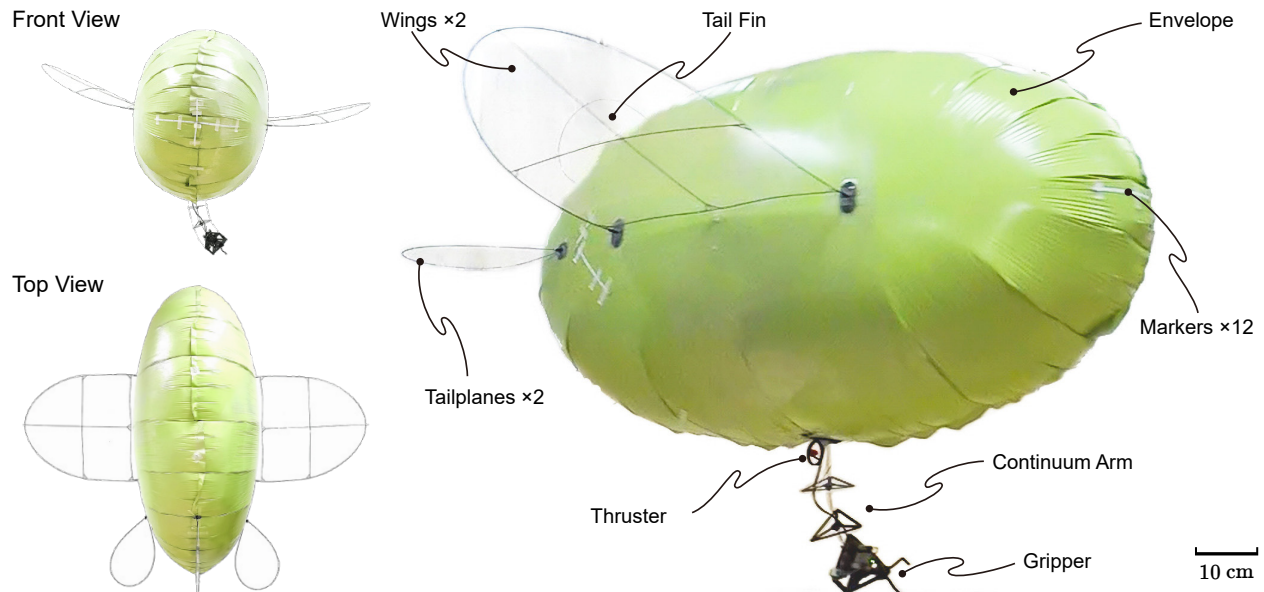


Fig. 12. The RGBlimp-Q prototype includes an envelope, a pair of main wings, a tail fin, two tailplanes, and the continuum arm with a battery. The left parts display the prototype in front view and top view. The right part shows the components, taken during a flight trial.

stationary mass m , encompassing an envelope, wings, and motion capture markers, as illustrated in Fig. 12. The mass distribution of the RGBlimp-Q prototype is detailed in Table I.

TABLE I
MASS DISTRIBUTION OF THE RGBLIMP-Q PROTOTYPE.

Component	Weight
Buoyant Lift ^a $-F_b$ (Helium)	-194.23 gf
Stationary Mass m_0	108.69 g
Helium	26.93 g
Envelop	53.74 g
Main Wings	$8.33 \text{ g} \times 2$
Tail Wings (Tail Fin & Tailplanes)	$2.79 \text{ g} \times 3$
Motion Capture Markers (Infrared LEDs)	2.98 g
Moving Mass m_a	92.21 g
Battery	10.42 g
Continuum Arm	81.79 g
Total Weight (Net ^b)	6.67 g

^aThe total buoyancy from helium in gram force (gf). ^bThe total net weight stands for the weight remaining after deducting buoyancy, i.e., $m_0 + m_a - F_b$.

The envelope consists of an ellipsoidal mylar balloon filled with approximately 160 liters of helium, providing a total buoyant lift of 194.23 gf. The main wings and tail wings, which include a tail fin and two tailplanes, contribute to both aerodynamic lift and attitude stability. The main wings, similar to those in our previous work [7], feature a 400 mm wingspan and a 15 deg dihedral angle, adopting an aerodynamic shape. The tail fin is mounted vertically on the tail section of the envelope, while the pair of tailplanes is mounted horizontally. The motion capture markers, comprising 850 nm infrared LEDs, facilitate indoor motion capture experiments.

C. Experimental Setup and System Identification

The inertia tensor is calculated from the CAD model, yielding $\mathbf{J} = \text{diag}(0.035, 0.020, 0.015) \text{ kg} \cdot \text{m}^2$. The gravitational constant is set to $g = 9.81 \text{ m/s}^2$. Utilizing the identification approach introduced in our previous work [7], the parameters in Eq. (37) are identified, as listed in Table II.

TABLE II
IDENTIFIED AERODYNAMIC COEFFICIENTS OF THE PROTOTYPE.

C_{\square}^*	0	α	β
D	0.243	8.838 rad^{-2}	9.016 rad^{-2}
S	-0.082	-0.285 rad^{-2}	-2.356 rad^{-1}
L	0.159	2.938 rad^{-1}	8.103 rad^{-2}
M_1	-0.036	0.553 rad^{-1}	-0.683 rad^{-1}
M_2	0.057	0.093 rad^{-1}	5.236 rad^{-2}
M_3	0.093	-0.209 rad^{-1}	-0.356 rad^{-1}
K_1, K_2, K_3	-0.073, -0.052, -0.032	$\text{N} \cdot \text{m} \cdot \text{s/rad}$	

* Due to space constraints, the degree of the corresponding term in the aerodynamic coefficient is inferred from its unit, e.g., $C_D^0 \alpha^2 = (8.838 \text{ rad}^{-2}) \cdot \alpha^2$.

The flight performance of the RGBlimp-Q prototype is evaluated through numerous flight trials conducted in both indoor and outdoor settings. Indoor flights take place within a motion capture arena measuring $L10.0 \times W6.0 \times H3.0 \text{ m}$, equipped with ten *OptiTrack* cameras. These cameras capture data at 60 Hz with an accuracy of 0.8 mm RMS in position

estimation error. For outdoor flights, a side-view camera and an overhead camera, positioned 7 m above the ground, are used to record flight trajectories. Each trial, whether indoor or outdoor, utilizes an electromagnetic releaser to ensure stability and consistency in the starting pose. Communication between the robot and the host PC occurs via a router and ROS.

V. EXPERIMENT AND DISCUSSION

In this section, we present the results of flight experiments conducted with the prototype and its comparison counterparts. Through these experiments, we evaluate the effectiveness of the design in achieving enhanced attitude adjustment and energy efficiency.

A. Flight Maneuverability Experiment

The proposed continuum-based moving mass actuation enables agile attitude maneuvers with less reliance on aerodynamics, as experimentally demonstrated below.

1) *Adjusting pitch-roll angles under zero propulsion*: with the propeller shutdown and the RGBlimp-Q floating in the air, the continuum arm was controlled by the PID controller following predefined alternating sinusoidal control inputs, i.e., (δ_x^*, δ_y^*) , as shown in Fig. 13(b). As a result, the continuum arm alternately moved the same distance along the x_b or y_b directions, thus the end motion trajectory of the continuum arm formed a rectangle, as shown in Fig. 13(a).

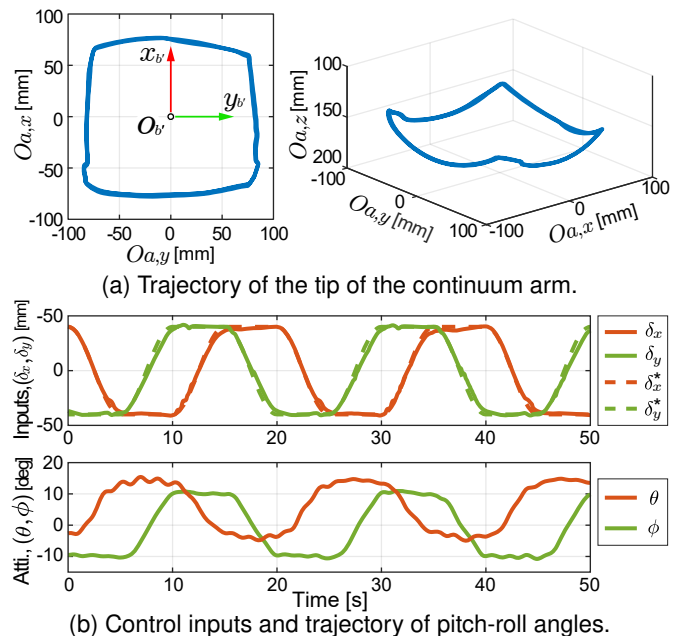


Fig. 13. Experimental results of pitch-roll adjustment through the moving mass control of the continuum arm in static floating state without propulsion. (a) Square-like trajectory of the continuum arm tip (moving mass m_a), with its four corners tilted up. (b) Trajectories of alternating sinusoidal control inputs (δ_x, δ_y) and corresponding attitude outputs pitch-roll angles (θ, ϕ) . The experimental results demonstrate the effectiveness of the moving mass control in attitude adjustment, even without aerodynamic moments and propulsion.

Figure 13 presents pitch-roll angles of the RGBlimp-Q prototype adjusted by the motion of the continuum arm. It is observed that the inner loop control successfully tracks

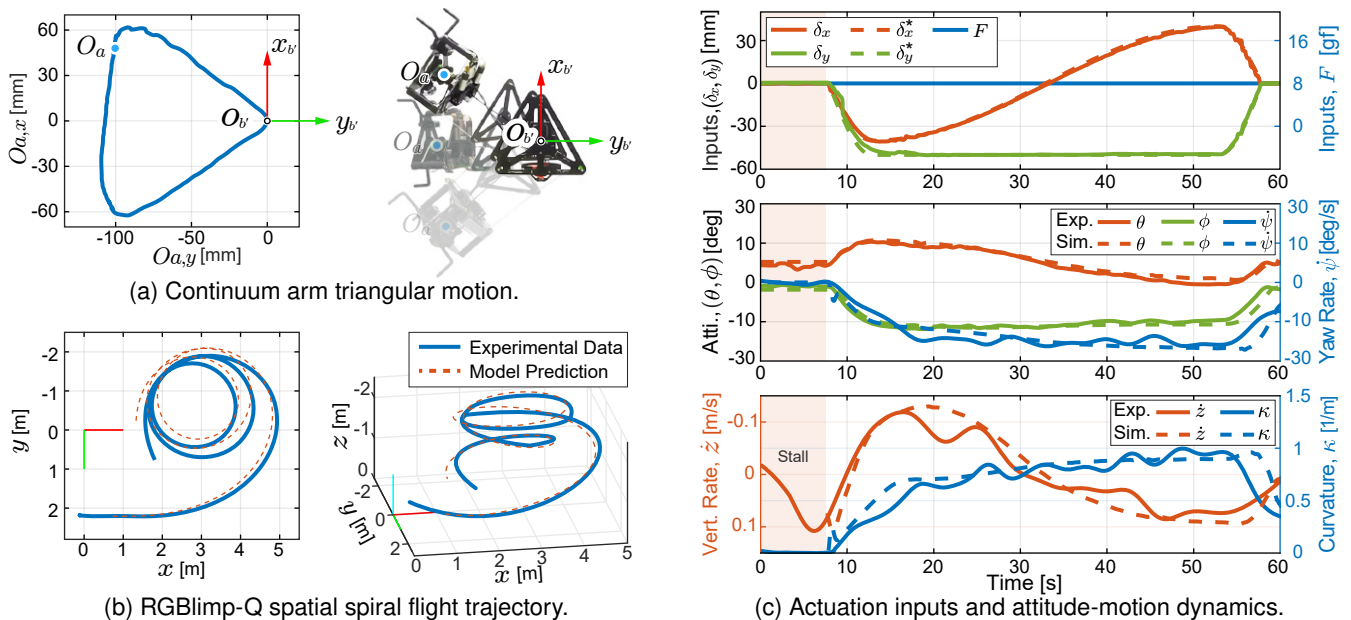


Fig. 14. Experimental results and model predictions of the dynamic flight under time-varying continuum arm inputs. The triangular motion of continuum-based moving mass O_a results in a spiral flight trajectory with attitude-motion dynamics. (a) The continuum arm, following predefined control inputs, forms a triangular trajectory. (b) The flight trajectory of the robot exhibits varying curvature in the horizontal projection and varying speed in the vertical plane. (c) Top: the continuum arm (δ_x, δ_y) tracks a piecewise trigonometric function (δ_x^*, δ_y^*) . Mid: pitch θ and roll ϕ depend on (δ_x, δ_y) , and yaw rate $\dot{\psi}$ depends on ϕ . Bottom: vertical speed V_z and curvature κ are influenced by θ and ϕ via aerodynamic forces. Model predictions (\dot{z}, κ) for the take-off phase (0-8 seconds) are omitted because the stall AoA α is incompatible with the aerodynamic model.

the desired continuum arm configuration (δ_x^*, δ_y^*) . Further, the input (δ_x, δ_y) independently controls the pitch and roll angles.

2) *Maneuvering flight with moving mass control*: During flight, the RGBlimp-Q adjusts its direction and altitude by controlling aerodynamic yaw moment and lift through roll and pitch angle adjustments.

Figure 14 illustrates the experimental results of the maneuvering flight along with model predictions. The inputs, forming a triangular motion of continuum-based moving mass O_a (Fig. 14(a)), result in a spiral flight trajectory with time-varying altitude and curvature (Fig. 14(b)). The pitch θ and roll ϕ are individually adjusted by the inputs δ_x and δ_y , respectively. Despite low cruising speed about 0.5 m/s, aerodynamic lift and yaw moment vary with θ and ϕ , respectively, affecting vertical speed V_z and yaw rate $\dot{\psi}$.

B. Flight Robustness Experiment

1) *Flight with a robust course direction (yaw angle $\psi^*=0$)*: extensive indoor and outdoor trials comparing open-loop and feedback control with moving mass actuation were conducted to demonstrate the flight robustness of the RGBlimp-Q against wind disturbances. These experiments focused on regulating the yaw angle to maintain a steady course direction.

For indoor flights, the experimental setup resembled that depicted in Fig. 15(c). An electric fan (specifically, the *Dyson AM07 tower fan*) was adopted to create environmental wind disturbances at varying intensity levels. Three levels of wind intensity were considered, corresponding to average wind speeds of approximately 0.0, 1.0, and 1.7 m/s, respectively. Each level was tested five times, with trials consisting of

both open-loop flights with predefined control and closed-loop flights with feedback control.

The comparison results of the yaw angles along with the feedback control inputs are illustrated in Fig. 15(a). It is worthy noting that as the wind level increases, the open-loop flight trajectory reached the boundaries of the flight area prematurely, resulting in significantly shorter flight time. It is observed that the input δ_y (green lines in the second row) effectively adjusts the roll angle ϕ (green lines in the first row), leading to further control of the flight heading angle ψ by leveraging the coupling between the aerodynamic yaw moment and the roll angle ϕ . In scenarios without environmental wind disturbance, the heading angle in open-loop flights tends to drift due to inevitable asymmetries in our prototype development. The introduction of moving mass control dramatically helps mitigate this problem, ensuring flight robustness. When encountering environmental winds during flight, the moving mass control based on the continuum arm demonstrates a rapid response and effective disturbance rejection.

As shown in Fig. 15(b), the flight trajectories are compared to highlight feedback yaw control with moving mass actuation versus open-loop flight under fan-generated wind disturbances, along with CFD-simulated wind direction for reference. The experimental results demonstrate that a robust flight attitude is the foundation for trajectory tracking.

For outdoor flights, a balloon was set up to indicate the direction and intensity of the natural wind, as shown in Fig. 16(a). The wind speed varied between 0.5 m/s and 1.5 m/s with gusts up to 3 m/s, with the wind blowing from *South* to *North*. Defining $\psi = 0$ as westward with clockwise rotations positive, open-loop and closed-loop flights from *East*

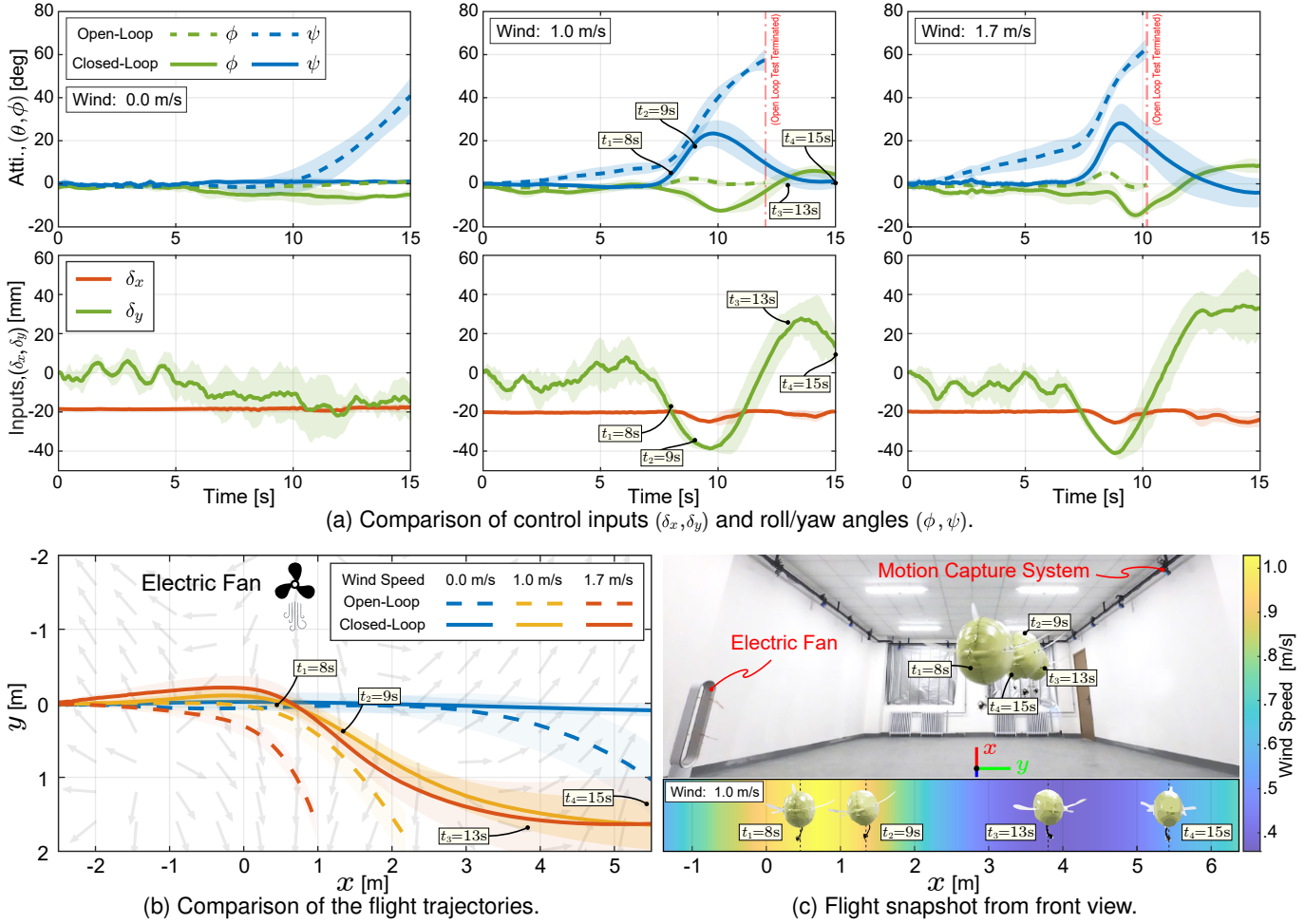
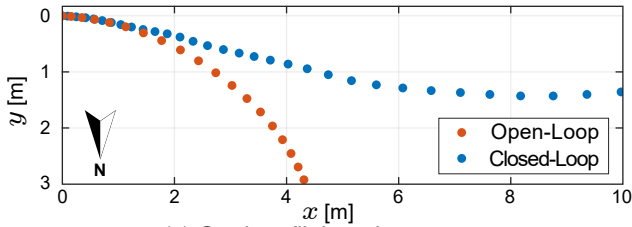


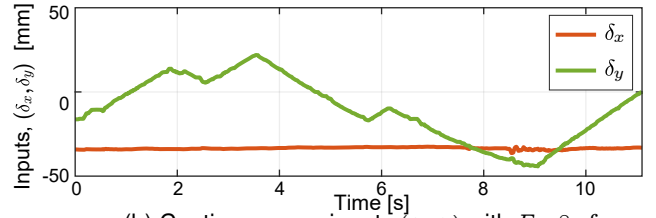
Fig. 15. Experimental results of the indoor flight trials under fan-generated wind disturbances. (a) Comparison of yaw angle regulation $\psi^* = 0$ under varying wind disturbances at levels 0.0, 1.0, and 1.7 m/s: feedback control with moving mass actuation vs. open-loop flight in indoor trials, shaded areas indicating deviations. The first row compares the attitude (ϕ, ψ) in closed-loop (solid lines) and open-loop (dashed lines) flights, with the pitch angle held constant at $\theta \approx 13^\circ$. The second row shows inputs (δ_x, δ_y) for closed-loop attitude control, while open-loop inputs are fixed at $(\delta_x^{\text{ol}}, \delta_y^{\text{ol}}) = (-20, 0)$ mm. (b) Comparison of flight trajectories highlights feedback yaw control with moving mass actuation (solid lines) versus open-loop flight (dashed lines) under fan-generated wind disturbances, demonstrating robust flight attitude as the foundation for trajectory tracking. Meanwhile, selected snapshot positions and CFD-simulated wind direction distribution are presented for reference. (c) Wind-disturbed motion arena setup: CFD-generated speed heat maps with continuum arm dynamic response snapshots.



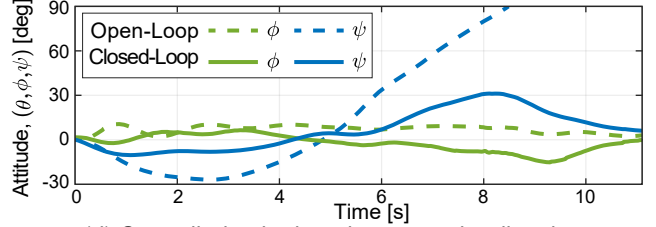
(a) Flight snapshot from side and top views.



(c) Outdoor flight trajectory.



(b) Continuum arm inputs (δ_x, δ_y) with $F = 8$ gf.



(d) Controlled attitude trajectory under disturbances.

Fig. 16. Experimental results of the outdoor flight tests under natural wind disturbance. (a) Closed-loop and open-loop outdoor flight trials, including side and top view snapshots and a balloon-based wind indicator. (b) The trajectories of control inputs for the closed-loop trial with respect to flight time. (c) Comparison of flight trajectories between open-loop and moving-mass-based yaw control under outdoor wind conditions. (d) Comparison of resulting yaw angles: feedback control with moving mass actuation vs. open-loop flight in outdoor trials. The outdoor experiments demonstrate that the control input of the continuum arm δ_y restores the heading angle of the robot ψ following a gust disturbance, confirming the effectiveness of our moving mass control design.

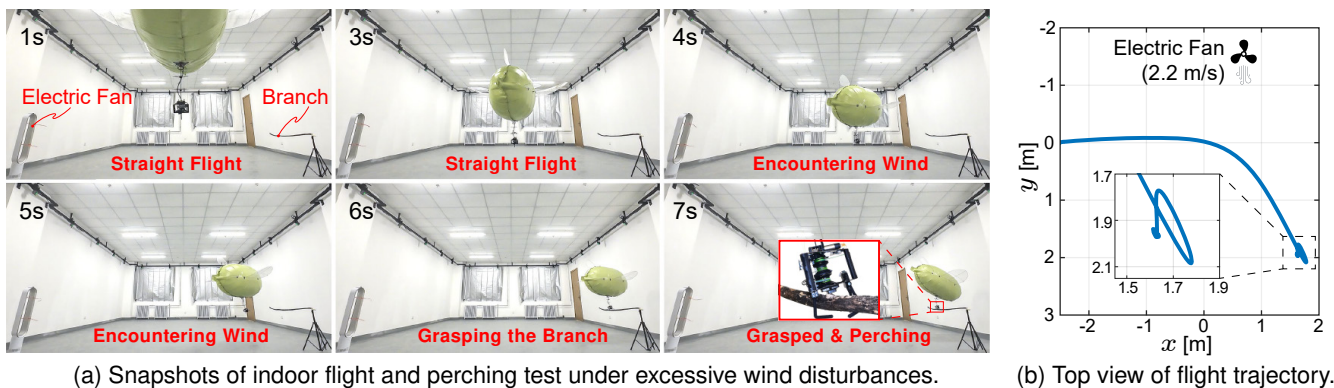


Fig. 17. Experimental results of the indoor flight and perching-on-branch test under excessive wind through the use of a bio-inspired claw for resisting wind disturbances. (a) The experimental snapshots illustrate the flight test process, starting from straight flight, encountering an excessive wind gust, and finally grasping a branch to resist the wind, mimicking bird behavior. (b) The top view of the flight trajectory recorded by the motion capture system, with a zoomed-in view of its final phase where the robot grasps the branch and maintains position in the excessive wind.

to *West* were conducted with a fixed thrust of $F = 8\text{ gf}$, producing the trajectories shown in Fig. 16(c). In closed-loop trials, the moving-mass-based feedback yaw controller regulated the yaw angle to compensate for wind disturbances.

In Fig. 16(b)(d), both the input δ_y and the roll angle ϕ exhibit similar variations, while the heading angle ψ shows an inverse trend. Specifically, when the heading angle ψ is disturbed, the moving mass control based on the proposed continuum arm adjusts the robot's roll angle ϕ to counteract the disturbance with the appropriate aerodynamic yaw moment. The attitude of the prototype did not fully converge to the desired zero angle by the end of the flight, with the heading reaching 6 deg. These results highlight the significant enhancement in attitude robustness achieved through the utilization of moving mass control based on the continuum arm, even in outdoor environments with complex wind disturbances.

2) *Grasping a branch for resisting excessive wind*: The effectiveness of a bio-inspired claw and associated grasping mechanism, akin to those used by birds, was demonstrated through a short flight against excessive wind (2.2 m/s) utilizing servo control based on predefined environmental priors and real-time external motion capture feedback. The key challenge of the perching-on-branch task is overcoming wind disturbances using the proposed bird-inspired continuum arm, enabling both aerial catching with the end-effector claw and flight attitude adjustment through moving mass actuation.

The flight, as depicted in Fig. 17, unfolded in three distinct phases, i.e., flying straight (0 s-3 s), encountering excessive wind (3 s-5 s), and finally, grasping a branch to resist the wind (5 s-7 s). Corresponding feedback control strategies were implemented in each phase to counteract wind disturbances, outlined as follows:

a) *Straight flight (0 s-3 s)*: The blimp initiated from a fixed position at the release point (electromagnetic releaser) and was controlled by the proposed dual-loop PID controller to fly along the positive x -axis direction, that is maintaining a stable course angle $\phi = 0$.

b) *Encountering strong wind (3 s-5 s)*: Upon entering the direct disturbance area of the electric fan, the heading angle was significantly deviated due to the wind disturbance. At this stage, the destination of the heading angle and relevant control

parameters of the dual-loop PID controller were updated to facilitate rapid adjustments in both attitude and altitude, aligning the end-effector claw with the predetermined branch grasping direction.

c) *Grasping a branch to resist wind (5 s-7 s)*: As the robot approached the known branch, the continuum arm was further adjusted to open the end-effector claw towards the effective grasping region based on the real-time spatial deviation. Once reaching the target, the gripper was closed to secure stable perching.

After being exposed to excessive wind, the robot quickly veered off to the side, then adjusted its attitude to navigate towards and ultimately grasp a branch for stability. In the enlarged plots of the final phase (grasping) shown in Fig. 17(b), the robot experienced a slight swing due to inertia after successfully grasping the branch, before stabilizing its position in the windy environment.

The perching-on-branch trials demonstrate a notable tolerance to uncertainties. This tolerance is facilitated by the effective graspable width of the gripper and the size of the effective grasping area of the target branch during the grasping process. More crucially, the moving-mass-based attitude adjustment mechanism, along with the passive compliance of the continuum arm's flexible end-effector, enhances the system's adaptability and adjustability to effectively address the grasping challenge.

The trials consisted of five attempts: two successful grasps and stable perches, one successful grasp followed by the gripper being blown away, and two failed attempts due to excessive turbulence. Consequently, the success rate of the trials was approximately 40%. This rate could be improved through refined control strategies and the inclusion of additional sensors, such as FPV or hand-eye cameras.

Additionally, we acknowledge that exposed cables in the current design may interact with or become entangled in environmental obstacles (e.g., small branches), indicating the need for further analysis and design improvement.

C. Comparison Against Other Actuation Mechanisms

The primary distinction of the proposed RGBlimp-Q lies in its novel actuation mechanism—continuum-based moving

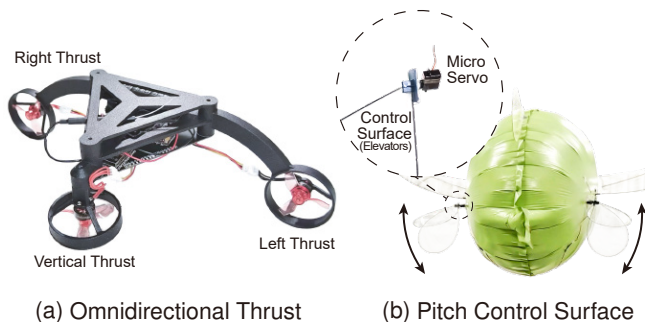


Fig. 18. Comparative baselines for actuation mechanisms. (a) Baseline Omni-Thrust Blimp: A reference prototype equipped with conventional omnidirectional thrusters, consisting of three BLDC propellers with electronic speed controllers (ESC), analogous to the forward thrust configuration of the RGBlimp-Q. This baseline system shares identical aerodynamic components (wings and envelope) and overall net weight with RGBlimp-Q, ensuring a fair comparison. (b) Pitch Control Surface: A baseline control-surface-based counterpart is configured by replacing the fixed tailplanes with elevators, allowing deflection within $\delta_e \in [-45^\circ, 45^\circ]$. While preserving the same overall configuration, this prototype utilizes aerodynamic moment generated by the elevator for pitch adjustment, actuated via micro servos.

mass actuation for flight attitude adjustment. This section conducts experimental comparisons and analyses of the RGBlimp-Q prototype and counterpart prototypes of the same aerodynamic and buoyant configuration but differing in actuation mechanisms: omnidirectional thrusters or control surfaces as shown in Fig. 18. To isolate the performance differences attributable solely to the actuation mechanisms, all flight experiments were conducted under standardized conditions. Specifically, all prototypes employed identical envelope and wing configurations (Fig. 12) and were tested in a consistent experimental environment, maintaining similar wind conditions, ambient temperature, and air pressure. Furthermore, the total net weight of all prototypes was precisely matched to $m = 6.67 \text{ g} \pm 0.30 \text{ g}$ using onboard ballast, as per Table I.

1) *Moving Mass vs. Omnidirectional Thrust—Attitude adjustment capability*: In alignment with the experimental setup employed in the indoor flight trials (Fig. 15(c)), comparative trials were conducted to assess the pitch-roll attitude adjustment capability of the RGBlimp-Q (moving mass actuation) and the conventional omnidirectional thrust actuation (Omni-Thrust). These trials were performed under identical wind disturbance conditions, specifically a crosswind of approximately 1.0 m/s , generated by a side-mounted electric fan. Both prototypes used a PID feedback controller for pitch-roll stabilization to assess performance differences in attitude regulation during flight.

The upper panel of Fig. 19 presents the cumulative root mean squared error (CumRMSE) of pitch-roll attitude, calculated as the sum of RMSE over time for both actuation mechanisms. The lower panel illustrates the corresponding inputs for RGBlimp-Q and Omni-Thrust, specifically the decoupled cable-driven continuum inputs (δ_x, δ_y) and the left-right omnidirectional thrust (F_l, F_r), respectively. The results show that within the crosswind disturbance (7-12 seconds), the roll CumRMSE for Omni-Thrust (dashed green line) increases sharply, whereas RGBlimp-Q (solid green line) shows a more gradual rise. Similarly, the pitch CumRMSE for RGBlimp-Q (solid red line) increases slowly, while Omni-Thrust (dashed

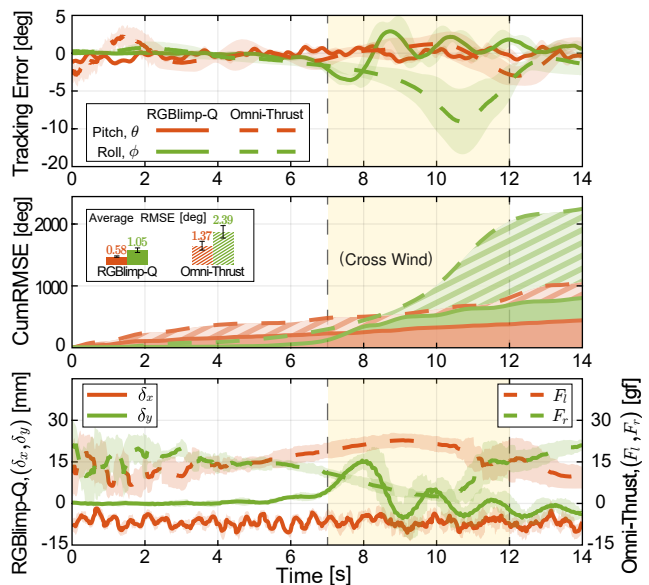


Fig. 19. The comparative results of flight with robust pitch-roll attitude, where the desired pitch angles are $\theta_R^* = 10^\circ$ for RGBlimp-Q and $\theta_O^* = 0$ for the Omni-Thrust prototype, and the desired roll angles are $\phi_R^* = \phi_O^* = 0$.

red line) exhibits a significant rise.

These trends demonstrate that while both systems are affected by crosswinds, the moving mass actuation in RGBlimp-Q mitigates long-term error accumulation in pitch and roll, ensuring better pitch-roll stability. The CumRMSE metric effectively highlights the advantages of moving mass actuation for robust attitude performance.

2) *Moving Mass vs. Omnidirectional Thrust—Flight energy efficiency*: To ensure a fair evaluation of the performance differences in flight energy efficiency between the actuation mechanisms, both prototypes are configured with identical propeller(s) and ESC(s) for thrust generation and are powered by the same driving unit (ESP32 SoC) and battery (7.4v, 150mAh, Li-Po). The primary difference in energy consumption arises from the actuation strategy. The proposed continuum-based moving mass actuation employs a single forward thrust and two actuators for pitch-roll attitude control. In contrast, the conventional omnidirectional thrust mechanism requires at least three thrust vectors—namely, left and right forward thrusts and a vertical thrust—resulting in increased energy expenditure.

The endurance performance comparison, evaluated in terms of flight time and distance, was conducted through continuous circling flights maintained at a consistent target altitude, velocity, and curvature until the battery could no longer support sustained flight. In each flight trial, the trajectory was recorded by the motion capture system. The corresponding results are presented in Fig. 20, with quantitative comparison metrics listed in Table III.

The comparison between the proposed RGBlimp-Q and the conventional omnidirectional blimp reveals significant performance improvements, particularly in energy efficiency, as measured by flight time and distance. At a comparable slow cruising speed of approximately 0.4 m/s (Fig. 20(a)), the proposed system exhibits nearly a twofold improvement in both flight duration and traveled distance. These enhance-

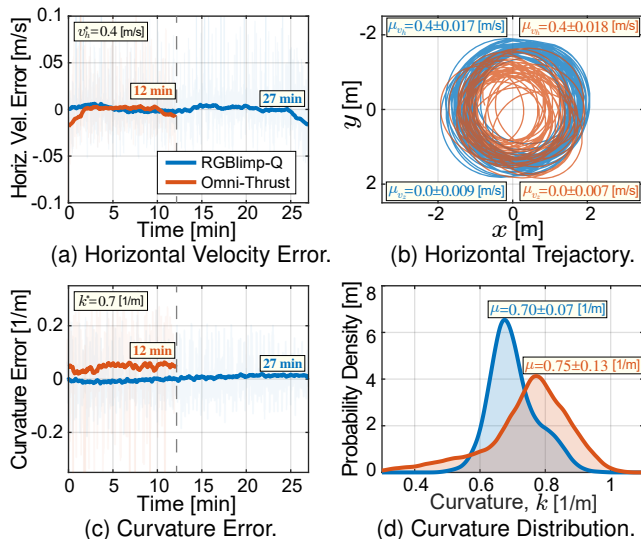


Fig. 20. Comparative results of flight endurance in terms of duration and distance between RGBlimp-Q and the Omni-Thrust prototype.

ments are attributed to significantly lower power consumption (5.6 mAh/min vs. 12.5 mAh/min), and a reduced energy-to-distance ratio (1.8 mWh/m vs. 4.0 mWh/m).

TABLE III
FLIGHT ENDURANCE PERFORMANCE: QUANTITATIVE COMPARISON BETWEEN THE RGBLIMP-Q AND OMNI-THRUST PROTOTYPE.

Metrics		RGBlimp-Q	Omni-Thrust
Time Duration	[min]	27	12
Trajectory Length	[m]	605	274
Horizontal Vel. STD	[m/s]	0.017	0.018
Vertical Vel. STD	[m/s]	0.009	0.007
Curvature STD	[1/m]	0.07	0.13
Power Rate	[mAh/min]	5.6	12.5
Specific Energy	[mWh/m]	1.8	4.0

As illustrated in Table III, the energy efficiency is demonstrated by a 125% increase in flight duration (27 min vs. 12 min), resulting from the moving mass actuation mechanism that effectively minimizes thrust loss by leveraging gravitational and aerodynamic moments. The RGBlimp-Q prototype also achieves a 2.21 longer flight path (605 m vs. 274 m) compared to the Omni-Thrust, while maintaining a more stable path curvature $\sigma_{\kappa}^R < \sigma_{\kappa}^O$. Curvature distribution analysis (Figs. 20(b)(c)(d)) shows a 46% reduction in standard deviation (0.07 m^{-1} vs. 0.13 m^{-1}), confirming the smoother trajectory enabled by the novel actuation mechanism.

These results highlight the significant enhancement in energy efficiency enabled by the proposed moving mass actuation mechanism in robotic blimps.

3) *Moving Mass vs. Control Surface—Flight attitude adjustment during low-speed flight:* Flight trials were conducted using prototypes with moving mass (RGBlimp-Q) and control surface actuation (Fig. 18(b)) under a fixed forward thrust of 7 gf. Step changes were applied to pitch-related control inputs: δ_x for moving mass actuation and δ_e for elevator deflection. In the initial phase of each trial, all control inputs were set to zero, i.e., $(\delta_x, \delta_y) = 0$ and $\delta_e = 0$. At $t = 6$ s, the pitch-related

inputs were step-changed to $\delta_x = -50 \text{ mm}$ and $\delta_e = -45 \text{ deg}$. Each configuration was tested over 10 repeated trials in an indoor motion environment with no wind disturbances, and the resulting pitch angle responses are presented in Fig. 21.

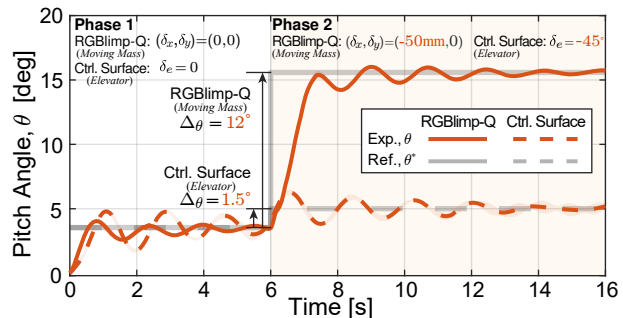


Fig. 21. Comparison results of pitch adjustment at low cruising speed using moving mass and control surface mechanisms. Pitch adjustment performance is evaluated under low-speed cruising conditions ($\|v\| = 0.8 \text{ m/s}$) in a no-wind environment.

The experimental results clearly demonstrate the superior performance of the moving mass actuation in regulating the pitch attitude of low-speed robotic blimps. Under identical control inputs, the moving mass prototype achieved a pitch angle change of approximately 12 deg, in contrast to the 1.5 deg change observed with the elevator-based system. This discrepancy is primarily attributed to the reduced effectiveness of aerodynamic moments at low flight speeds, which limits the authority of conventional control surfaces. Conversely, the moving mass mechanism leverages gravitational moments to induce substantial attitude changes, thereby enhancing control authority under low-speed conditions. These findings validate the effectiveness of the proposed moving mass actuation strategy in enabling agile and robust pitch control in robotic blimps operating in low-speed regimes.

D. Continuum Arm Reliability and Repeatability

To evaluate the working duration and tendon reliability of the cable-driven continuum mechanism, we conducted a cyclic motion test using a delicately designed experimental apparatus, as shown in Fig. 22. The platform comprises a continuum arm prototype identical in design, affixed to a lightweight carbon fiber rod mounted via a 2-DoF universal joint to a structural frame. This joint-link configuration emulates a pseudo buoyant envelope, where the support force N simulates buoyancy F_b , and the link length h represents the vertical distance from the pseudo-envelope's center of buoyancy (CB) to the base frame $O_{b'}-x_{b'}y_{b'}z_{b'}$ of the continuum arm, replicating the operational conditions of moving mass actuation, as illustrated in Fig. 4. Three actuation cables equipped with integrated tension sensors are continuously monitored via an NI USB-6212 analog input module to evaluate the mechanical load. Two IMUs are placed at both ends of the arm to estimate the system's attitude via an Extended Kalman Filter (EKF), from which the arm's configuration is computed in q -parametrization (δ_x, δ_y) . This configuration feeds into an inner-loop feedback controller to track time-varying reference inputs $(\delta_x^*(t), \delta_y^*(t))$ during repeated cycle motions.

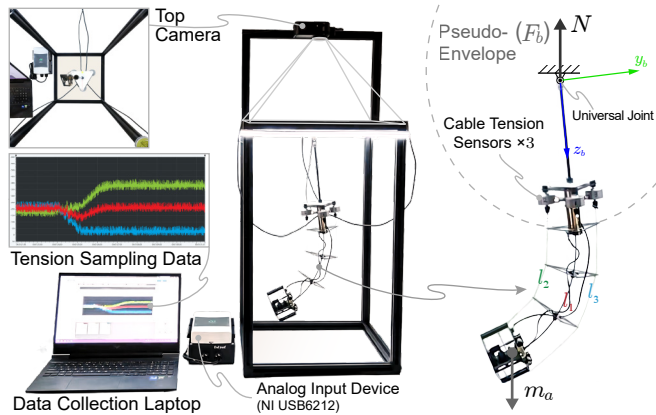


Fig. 22. Experimental setup for evaluating the reliability and repeatability of the continuum arm.

The test protocol involved sequential round-trip actuation from $q_{(0)}^* = (0, 0)$ to four directional configurations: front $q_{(1)}^* = (+50, 0)$ mm, right $q_{(2)}^* = (0, +50)$ mm, back $q_{(3)}^* = (-50, 0)$ mm, and left $q_{(4)}^* = (0, -50)$ mm, as illustrated in Fig. 23. This motion sequence was repeated for over 3000 round-trip cycles, covering all four directional axes, with a cumulative operation duration exceeding 18 hours.

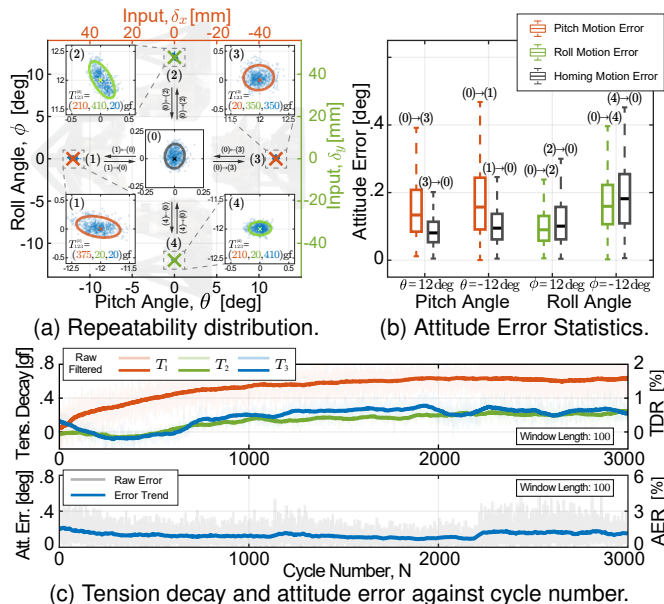


Fig. 23. Performance evaluation of the cable-driven continuum arm in terms of reliability and repeatability. (a) End-effector pitch-roll repeatability during repeated cycle motions between $\theta, \phi = \pm 12$ deg with homing motions, visualized using scatter plots and 2σ confidence ellipses; yielding mean standard deviations $\bar{\sigma}_\theta = 0.11$ deg, $\bar{\sigma}_\phi = 0.10$ deg. (b) Box plot of attitude errors across all trials, demonstrating tight variation bounds (≤ 0.3 deg), further validating high repeatability. (c) Reliability over 3000 actuation cycles, showing tension decay and attitude error trends via moving mean (window=100), confirming consistent performance.

Figure 23(a) illustrates pitch-roll repeatability during repeated cycle motions by plotting (θ, ϕ) and corresponding inputs (δ_x^*, δ_y^*) using zoomed-in scatter points and 2σ confidence ellipses for five configurations $q_{(k)}^*$, ($k=0, 1, 2, 3, 4$). The corresponding attitude of the pseudo-envelope: the pitch angles $\theta = \mp 12$ deg for $q_{(1)}^*, q_{(3)}^*$, the roll angle $\phi = \pm 12$ deg for $q_{(2)}^*, q_{(4)}^*$, and the initial attitude $\theta = \phi = 0$ for $q_{(0)}^*$. The repeatability test shows that (θ, ϕ) has pitch-roll mean standard

deviations of $\bar{\sigma}_\theta = 0.11$ deg and $\bar{\sigma}_\phi = 0.10$ deg. Additionally, the average tension $T_i^{(k)}$ ($i=1, 2, 3; k=1, 2, 3, 4$) for cables i at $q_{(k)}^*$ is provided.

Box-plot analysis in Fig. 23(b) further confirms the narrow distribution of attitude errors, consistently within ≤ 0.3 deg. These results validate the robustness of the proposed cable-driven design with the decoupled mechanism against tendon slacking and breakage. The system consistently achieves high repeatability in positioning, even under prolonged operation over extended durations and cycle counts. Overall, the continuum arm mechanism meets the stringent requirements for sustained, high-cycle performance necessary for moving-mass actuation in robotic gliding blimps.

As shown in Fig. 23(c), system reliability is evaluated based on cable tension degradation and attitude error trends. Cable l_1 showed a tension decay of 0.6 gf (1.8%), while cables l_2 and l_3 exhibited 0.3 gf (0.8%) reduction relative to initial values. Attitude errors remained within 0.2 deg (1%) for both pitch and roll throughout the test duration.

VI. CONCLUSION

In this article, we presented a comprehensive design of a bird-inspired robotic gliding blimp, termed RGBlimp-Q, engineered to exhibit enhanced maneuverability and resilience through the integration of an active continuum arm. This flying robot leverages the continuum arm for precise moving mass control, facilitating agile flight attitude maneuvers. In addition, the inclusion of a bionic claw at the end of the arm empowers the robot to grasp objects, akin to bird behavior, enabling it to withstand wind disturbances effectively. Extensive indoor and outdoor flight experiments were conducted, the results of which validated the effectiveness of the proposed design.

In future work, we will investigate more advanced control strategies such as model predictive control (MPC) and learning-based control to fully exploit the capabilities of the RGBlimp-Q. Autonomous perching and aerial manipulation, using onboard perception such as FPV or hand-eye cameras, will be developed through successive prototypes. Additionally, substantial optimization potential remains in the weight-strength trade-off. By selecting an optimized elasticity modulus for the continuum backbone, we can reduce the excessive strength margin, allowing low-density materials, such as foam-based composites, to effectively decrease both payload and buoyancy requirements. In addition, we will explore the integration of aerodynamic and buoyant lift mechanisms within a unified aerodynamically shaped envelope (e.g., a hybrid aerodynamic-buoyant flying wing), eliminating the need for additional wings. This approach will be investigated in subsequent iterations of the work.

In application, we envision deploying the RGBlimp-Q for real-world applications such as indoor or outdoor environmental monitoring and mapping, leveraging its enhanced durability and human-robot-interaction (HRI) safety to address diverse challenges. Moreover, it is worthwhile to explore aerial robotic manipulators that utilize the proposed bird-inspired continuum arm, applicable to both robotic blimps and rotary-wing aerial robots. Last but not least, robotic gliding blimps hold promise

as an aerial experimental platform for simulating and rapidly validating the design of underwater gliders, leveraging the similarity in dynamic mechanisms that combine aero-/hydro-dynamic lift with static buoyant lift.

ACKNOWLEDGMENTS

The authors would like to thank Prof. Zhongkui Li for his help in the motion capture experiment, and Zeyu Sha for help with the CFD simulation. The authors also gratefully acknowledge the reviewers and editors for their constructive comments and suggestions that greatly improved the quality of the manuscript.

APPENDIX

A. Proof of Invertibility of Matrix \mathbf{A} in Eq. (34)

We prove that the allocation matrix \mathbf{A} is invertible by analyzing the block matrix \mathbf{M} defined as:

$$\mathbf{M} = \begin{bmatrix} (m_0 + m_a)\mathbf{I} & -\mathbf{R}\mathbf{l}_g^\times \\ \mathbf{l}_g^\times \mathbf{R}^\mathbf{T} & \mathbf{J} - m_a(\mathbf{r}_a^\times)^2 \end{bmatrix}, \quad (\text{A.1})$$

where $\mathbf{A} = \mathbf{M}^{-1}$. The invertibility of \mathbf{A} is established through the application of the Schur complement and positive-definiteness properties.

Lemma 1. *The lower block $\mathbf{J}_{\text{eff}} = \mathbf{J} - m_a(\mathbf{r}_a^\times)^2$ is positive definite and invertible.*

Proof. First, the positive definiteness of the inertia matrix \mathbf{J} for the stationary mass m_0 is inherent in its definition, i.e.,

$$\mathbf{J} = \int_{m_0} (\|\mathbf{r}\|^2 \mathbf{I} - \mathbf{r}\mathbf{r}^\mathbf{T}) dm, \quad (\text{A.2})$$

where \mathbf{r} is the distance vector of dm with respect to the origin of the body-fixed frame. The operator $(\mathbf{r}_a^\times)^2$ is given by

$$(\mathbf{r}_a^\times)^2 = -\|\mathbf{r}_a\|^2 \mathbf{I} + \mathbf{r}_a \mathbf{r}_a^\mathbf{T}, \quad (\text{A.3})$$

which is symmetric. For any non-zero vector $\mathbf{x} \in \mathbb{R}^3$, we have

$$\begin{aligned} \mathbf{x}^\mathbf{T} (\mathbf{r}_a^\times)^2 \mathbf{x} &= -\|\mathbf{r}_a\|^2 \|\mathbf{x}\|^2 + (\mathbf{x}^\mathbf{T} \mathbf{r}_a)^2 \\ &\leq -\|\mathbf{r}_a\|^2 \|\mathbf{x}\|^2 + \|\mathbf{x}\|^2 \|\mathbf{r}_a\|^2 = 0. \end{aligned} \quad (\text{A.4})$$

Thus, $(\mathbf{r}_a^\times)^2$ is negative semi-definite. Consequently, the term $m_a(\mathbf{r}_a^\times)^2$ is also negative semi-definite, as $m_a > 0$. Therefore, $\mathbf{J}_{\text{eff}} = \mathbf{J} - m_a(\mathbf{r}_a^\times)^2$ represents the sum of a positive definite matrix and a positive semi-definite matrix. This guarantees that \mathbf{J}_{eff} is positive definite. Consequently, we have $\det(\mathbf{J}_{\text{eff}}) > 0$, confirming that \mathbf{J}_{eff} is invertible. \square

Lemma 2. *The Schur complement of \mathbf{J}_{eff} in \mathbf{M} is positive definite.*

Proof. The Schur complement \mathbf{S} of \mathbf{J}_{eff} is defined as

$$\mathbf{S} = (m_0 + m_a)\mathbf{I} + \mathbf{R}\mathbf{l}_g^\times \mathbf{J}_{\text{eff}}^{-1} \mathbf{l}_g^\times \mathbf{R}^\mathbf{T}. \quad (\text{A.5})$$

The first term $(m_0 + m_a)\mathbf{I}$ is positive definite. The second term $\mathbf{R}\mathbf{l}_g^\times \mathbf{J}_{\text{eff}}^{-1} \mathbf{l}_g^\times \mathbf{R}^\mathbf{T}$ is symmetric positive semi-definite, as $\mathbf{J}_{\text{eff}}^{-1}$ is positive definite. Therefore, we conclude that \mathbf{S} is positive definite, and $\det(\mathbf{S}) > 0$. \square

Theorem 1. *The matrix \mathbf{M} in Eq. (A.1) is invertible, and therefore the allocation matrix $\mathbf{A} = \mathbf{M}^{-1}$ exists.*

Proof. Using the Schur complement formula, the determinant of \mathbf{M} is given by

$$\det(\mathbf{M}) = \det(\mathbf{J}_{\text{eff}}) \det(\mathbf{S}). \quad (\text{A.6})$$

From Lemmas 1 and 2, we know that $\det(\mathbf{J}_{\text{eff}}) > 0$ and $\det(\mathbf{S}) > 0$. Therefore, it follows that $\det(\mathbf{M}) > 0$, establishing that \mathbf{M} is invertible. Consequently, the allocation matrix $\mathbf{A} = \mathbf{M}^{-1}$ is well-defined. \square

REFERENCES

- [1] A. Ollero, M. Tognon, A. Suarez *et al.*, "Past, present, and future of aerial robotic manipulators," *IEEE Trans. Robot.*, vol. 38, no. 1, pp. 626–645, 2021.
- [2] H. Zhong, J. Liang, Y. Chen, H. Zhang, J. Mao, and Y. Wang, "Prototype, modeling, and control of aerial robots with physical interaction: A review," *IEEE Trans. Autom. Sci. Eng.*, pp. 1–15, 2024.
- [3] F. Ruggiero, V. Lippiello, and A. Ollero, "Aerial manipulation: A literature review," *IEEE Robot. Autom. Lett.*, vol. 3, no. 3, pp. 1957–1964, 2018.
- [4] S. H. Song, G. Y. Yeon, H. W. Shon *et al.*, "Design and control of soft unmanned aerial vehicle "s-cloud"," *IEEE/ASME Trans. Mech.*, vol. 26, no. 1, pp. 267–275, 2021.
- [5] V. Mai, M. Kamel, M. Krebs *et al.*, "Local positioning system using ubw range measurements for an unmanned blimp," *IEEE Robot. Autom. Lett.*, vol. 3, no. 4, pp. 2971–2978, 2018.
- [6] C. Lu, C. Huang, J. Huang *et al.*, "A heterogeneous unmanned ground vehicle and blimp robot team for search and rescue using data-driven autonomy and communication-aware navigation," *Field Robot.*, vol. 2, pp. 557–594, 2022.
- [7] H. Cheng, Z. Sha, Y. Zhu, and F. Zhang, "RGBlimp: Robotic Gliding Blimp-design, modeling, development, and aerodynamics analysis," *IEEE Robot. Autom. Lett.*, 2023.
- [8] M. González-Álvarez, J. Dupeyroux, F. Corradi *et al.*, "Evolved neuro-morphic radar-based altitude controller for an autonomous open-source blimp," in *Proc. IEEE Int. Conf. Robot. and Autom.*, 2022, pp. 85–90.
- [9] J. Muller, A. Rottmann, L. M. Reindl *et al.*, "A probabilistic sonar sensor model for robust localization of a small-size blimp in indoor environments using a particle filter," in *Proc. IEEE Int. Conf. Robot. and Autom.*, 2009, pp. 3589–3594.
- [10] H. S. Poon, M. K. K. Lam, M. Chow *et al.*, "Noiseless and vibration-free ionic propulsion technology for indoor surveillance blimps," in *Proc. IEEE Int. Conf. Robot. and Autom.*, 2009, pp. 2891–2896.
- [11] J. Xu, D. S. D'antonio, D. J. Ammirato, and D. Saldaña, "SBLimp: Design, model, and translational motion control for a swing-blimp," in *Proc. IEEE/RSJ Int. Conf. Intell. Robots Syst.*, 2023, pp. 6977–6982.
- [12] T. Fukao, T. Oshibuchi, K. Osuka *et al.*, "Outdoor blimp robots for rescue surveillance systems," in *Proc. SICE Annual Conf.*, 2008, pp. 982–987.
- [13] S. Sharma, M. Verhoeff, F. Joosen *et al.*, "A morphing quadrotor-blimp with balloon failure resilience for mobile ecological sensing," *IEEE Robot. Autom. Lett.*, vol. 9, no. 7, pp. 6408–6415, 2024.
- [14] H. Ishida, "Blimp Robot for Three-Dimensional Gas Distribution Mapping in Indoor Environment," *AIP Conf. Proc.*, vol. 1137, no. 1, pp. 61–64, 05 2009.
- [15] C. F. Liew and T. Yairi, "Quadrotor or blimp? noise and appearance considerations in designing social aerial robot," in *Proc. ACM/IEEE Int. Conf. Hum.-Robot Interaction*, 2013, pp. 183–184.
- [16] M. Hou, Q. Tao, and F. Zhang, "Human pointing motion during interaction with an autonomous blimp," *Sci. Rep.*, vol. 12, no. 1, p. 11402, 2022.
- [17] N. Yao, E. Anaya, Q. Tao *et al.*, "Monocular vision-based human following on miniature robotic blimp," in *Proc. IEEE Int. Conf. Robot. Autom.* IEEE, 2017, pp. 3244–3249.
- [18] M. Burri, L. Gasser, M. Käch *et al.*, "Design and control of a spherical omnidirectional blimp," in *Proc. IEEE/RSJ Int. Conf. Intell. Robot. Syst.*, 2013, pp. 1873–1879.
- [19] D. St-Onge, C. Gosselin, and N. Reeves, "Dynamic modelling and control of a cubic flying blimp using external motion capture," *J. Syst. and Contr. Eng.*, vol. 229, no. 10, pp. 970–982, 2015.

- [20] R. Lakhmani, “Kingfisher knocks bird off branch after flying into it.” Accessed: Apr. 2024, [Online]. Available: <https://youtu.be/QQvOjNKXKSU>.
- [21] Y. Wang, G. Zheng, D. Efimov *et al.*, “Disturbance compensation based control for an indoor blimp robot,” in *Proc. IEEE Int. Conf. Robot. Autom.*, 2019, pp. 2040–2046.
- [22] —, “Improved altitude control method with disturbance compensation for an indoor blimp robot,” in *Proc. IEEE Conf. Decision Control*, 2017, pp. 3902–3907.
- [23] Y. T. Liu, E. Price, M. J. Black *et al.*, “Deep residual reinforcement learning based autonomous blimp control,” in *Proc. IEEE/RSJ Int. Conf. Intell. Robot. Syst.*, 2022, pp. 12 566–12 573.
- [24] H. Kawano, “Method for designating the wind condition in MDP-based motion planning of under-actuated blimp type uav,” in *Proc. IEEE Int. Conf. Robot. Autom.*, 2007, pp. 1049–1055.
- [25] B. Wang, Z. Ma, S. Lai *et al.*, “Neural moving horizon estimation for robust flight control,” *IEEE Trans. Robot.*, vol. 40, pp. 639–659, 2024.
- [26] A. Saviolo, J. Frey, A. Rathod *et al.*, “Active learning of discrete-time dynamics for uncertainty-aware model predictive control,” *IEEE Trans. Robot.*, vol. 40, pp. 1273–1291, 2024.
- [27] M. O’Connell, G. Shi, X. Shi *et al.*, “Neural-fly enables rapid learning for agile flight in strong winds,” *Sci. Robot.*, vol. 7, no. 66, p. eabm6597, 2022.
- [28] C. Powers, D. Mellinger, A. Kushleyev, B. Kothmann, and V. Kumar, “Influence of aerodynamics and proximity effects in quadrotor flight,” in *Experimental Robotics*. Springer, 2013, pp. 289–302.
- [29] Q. Tao, J. Wang, Z. Xu *et al.*, “Swing-reducing flight control system for an underactuated indoor miniature autonomous blimp,” *IEEE/ASME Trans. Mech.*, vol. 26, no. 4, pp. 1895–1904, 2021.
- [30] P. C. Khandelwal and T. L. Hedrick, “Combined effects of body posture and three-dimensional wing shape enable efficient gliding in flying lizards,” *Sci. Rep.*, vol. 12, no. 1, p. 1793, 2022.
- [31] K. L. Bishop, “The relationship between 3-D kinematics and gliding performance in the southern flying squirrel, *glaucomys volans*,” *J. Exp. Biol.*, vol. 209, no. 4, pp. 689–701, 2006.
- [32] C. Harvey, V. Baliga, J. Wong *et al.*, “Birds can transition between stable and unstable states via wing morphing,” *Nature*, vol. 603, no. 7902, pp. 648–653, 2022.
- [33] R. Brown, “The flight of birds,” *Biol. Rev.*, vol. 38, no. 4, pp. 460–489, 1963.
- [34] W. R. Roderick, M. R. Cutkosky, and D. Lentink, “Bird-inspired dynamic grasping and perching in arboreal environments,” *Sci. Robot.*, vol. 6, no. 61, p. eabj7562, 2021.
- [35] “The brown-backed shrike in the wind,” Accessed: Apr. 2024, [Online]. Available: <https://www.bilibili.com/video/BV1BW4y1n75r>.
- [36] W. D. Shin, H.-V. Phan, M. A. Daley, A. J. Ijspeert, and D. Floreano, “Fast ground-to-air transition with avian-inspired multifunctional legs,” *Nature*, vol. 636, no. 8041, pp. 86–91, 2024.
- [37] K. Hang, X. Lyu, H. Song *et al.*, “Perching and resting—a paradigm for uav maneuvering with modularized landing gears,” *Sci. Robot.*, vol. 4, no. 28, p. eaau6637, 2019.
- [38] H. Paul, K. Ono, R. Ladig *et al.*, “A multirotor platform employing a three-axis vertical articulated robotic arm for aerial manipulation tasks,” in *Proc. IEEE/ASME Int. Conf. Adv. Intell. Mech.*, 2018, pp. 478–485.
- [39] J. Thomas, J. Polin, K. Sreenath *et al.*, “Avian-inspired grasping for quadrotor micro uavs,” in *Proc. ASME Int. Des. Eng. Tech. Conf. and Comp. Inf. Eng. Conf.*, vol. 55935, 2013, p. V06AT07A014.
- [40] W. Stewart, E. Ajanic, M. Müller *et al.*, “How to swoop and grasp like a bird with a passive claw for a high-speed grasping,” *IEEE/ASME Trans. Mech.*, vol. 27, no. 5, pp. 3527–3535, 2022.
- [41] S. Kolachalama, S. Lakshmanan *et al.*, “Continuum robots for manipulation applications: A survey,” *J. Robot.*, vol. 2020, 2020.
- [42] G. Robinson and J. B. C. Davies, “Continuum robots—a state of the art,” in *Proc. IEEE Int. Conf. Robot. Autom.*, vol. 4, 1999, pp. 2849–2854.
- [43] M. Russo, S. M. H. Sadati, X. Dong, A. Mohammad, I. D. Walker *et al.*, “Continuum robots: An overview,” *Adv. Intel. Syst.*, vol. 5, no. 5, p. 2200367, 2023.
- [44] M. Coad, L. Blumenschein, S. Cutler *et al.*, “Vine robots: Design, teleoperation, and deployment for navigation and exploration,” *IEEE Robot. Autom. Magaz.*, vol. PP, 10 2019.
- [45] R. K. Katzschmann, C. Della Santina, Y. Toshimitsu *et al.*, “Dynamic motion control of multi-segment soft robots using piecewise constant curvature matched with an augmented rigid body model,” in *Proc. IEEE Int. Conf. Soft Robot.*, 2019, pp. 454–461.
- [46] S. Huang, D. Meng, X. Wang *et al.*, “A 3D static modeling method and experimental verification of continuum robots based on pseudo-rigid body theory,” in *Proc. IEEE/RSJ Int. Conf. Intell. Robots Syst.*, 2019, pp. 4672–4677.
- [47] G. Fang, Y. Tian, Z.-X. Yang *et al.*, “Efficient jacobian-based inverse kinematics with sim-to-real transfer of soft robots by learning,” *IEEE/ASME Trans. Mech.*, vol. 27, no. 6, pp. 5296–5306, 2022.
- [48] H. Cheng, H. Liu, X. Wang *et al.*, “Approximate piecewise constant curvature equivalent model and their application to continuum robot configuration estimation,” in *Proc. IEEE Int. Conf. Syst. Man Cyber.*, 2020, pp. 1929–1936.
- [49] B. A. Jones and I. D. Walker, “Kinematics for multisection continuum robots,” *IEEE Trans. Robot.*, vol. 22, no. 1, pp. 43–55, 2006.
- [50] C. Della Santina, A. Bicchi, and D. Rus, “On an improved state parametrization for soft robots with piecewise constant curvature and its use in model based control,” *IEEE Robot. Autom. Lett.*, vol. 5, no. 2, pp. 1001–1008, 2020.
- [51] H. Cheng, H. Xu, H. Shang *et al.*, “Orientation to pose: Continuum robots shape reconstruction based on the multi-attitude solving approach,” in *Proc. IEEE Int. Conf. Robot. Autom.*, 2022, pp. 3203–3209.
- [52] R. Peng, Z. Wang, and P. Lu, “Aecom: An aerial continuum manipulator with imu-based kinematic modeling and tendon-slacking prevention,” *IEEE Trans. Syst. Man Cybern.*, vol. 53, no. 8, pp. 4740–4752, 2023.
- [53] R. Peng, Y. Wang, M. Lu, and P. Lu, “A dexterous and compliant aerial continuum manipulator for cluttered and constrained environments,” *Nature Communications*, vol. 16, no. 1, p. 889, 2025.
- [54] R. F. Stengel, *Flight Dynamics: Second Edition*. Princeton University Press, 2022.



Hao Cheng received the Bachelor’s degree in New Energy Science and Engineering (Wind Power) from North China Electric Power University, China, in 2017, and the Master’s degree in Control Engineering from Tsinghua University, China, in 2021. He is currently working toward the Ph.D. degree in Mechanics at Peking University, China, under the supervision of Prof. F. Zhang. His research interests include Light-Than-Air Aerial Vehicles, Bioinspired Robotics, and Continuum Robots.



Feitian Zhang received the Bachelor’s and Master’s degrees in Automatic Control from Harbin Institute of Technology, Harbin, China, in 2007 and 2009, respectively, and the Ph.D. degree in Electrical and Computer Engineering from Michigan State University, East Lansing, MI, in 2014.

Feitian Zhang is currently an Associate Professor in the School of Advanced Manufacturing and Robotics at Peking University. Prior to joining Peking University, he was an Assistant Professor in the Department of Electrical and Computer Engineering at George Mason University (GMU), Fairfax, VA, and the founding director of the Bioinspired Robotics and Intelligent Control Laboratory (BRICLab) from 2016 to 2021. His research interests include Bioinspired Robotics, Control Systems, Artificial Intelligence, Underwater Vehicles, and Aerial Vehicles.